Nature Communications

https://doi.org/10.1038/s41467-026-71572-z

Article in Press

Flexible, large-area, recyclable, decoupled dual sensing of temperature and pressure enabled by mechanically-electrically hybrid networks

Received: 22 July 2025

Accepted: 23 March 2026

Cite this article as: Zhu, J., Liu, X., Li, J. *et al.* Flexible, large-area, recyclable, decoupled dual sensing of temperature and pressure enabled by mechanically-electrically hybrid networks. *Nat Commun* (2026). https://doi.org/10.1038/s41467-026-71572-z

Jia Zhu, Xionghao Liu, Jiaying Li, Yang Xiao, Xin Mu, Ying Chen, Haibin Liu, Yujiao Qin, Yuhua Cheng, Zhenlong Huang, Min Gao, Taisong Pan, Jian Yang, Huanyu Cheng & Yuan Lin

Flexible, Large-area, Recyclable, Decoupled Dual Sensing of Temperature and Pressure Enabled by Mechanically-Electrically Hybrid Networks

*Jia Zhu[1, 2, 3 *], Xionghao Liu[1], Jiaying Li[1], Yang Xiao[1], Xin Mu[1], Ying Chen[4], Haibin Liu[4], Yujiao Qin[4], Yuhua Cheng[5], Zhenlong Huang[1], Min Gao[1], Taisong Pan[1], Jian Yang[6], Huanyu Cheng[7 *], Yuan Lin[1, 8 *]*

[1] School of Materials and Energy, University of Electronic Science and Technology of China, Chengdu 611700, P. R. China

[2] Yangtze Delta Region Institute (Quzhou), University of Electronics Science and Technology of China, Quzhou 324000, P. R. China

[3] Energy and Information Materials Key Laboratory of Sichuan Province, University of Electronic Science and Technology of China, Chengdu 611731, P. R. China

[4] College of Mechanical and Energy Engineering, Beijing University of Technology, Beijing 100124, P. R. China

[5] School of Automation Engineering, University of Electronic Science and Technology of China, Chengdu 611700, P. R. China

[6] Department of Materials Science and Engineering, School of Engineering, Westlake University, Hangzhou, Zhejiang 310030, P. R. China

[7] Department of Engineering Science and Mechanics, The Pennsylvania State University, University Park, Pennsylvania 16802, USA

[8] Medico-Engineering Cooperation on Applied Medicine Research Center, University of Electronics Science and Technology of China, Chengdu 611700, P. R. China

[*]To whom correspondence should be addressed. E-mail: zhujia1990@uestc.edu.cn (J.Z.), huanyu.cheng@psu.edu (H.C.), and linyuan@uestc.edu.cn (Y.L.).

Abstract

Thin, conformable electronic skin (e-skin), capable of accurately perceiving various stimuli (e.g., temperature and pressure), is an important building block for various cutting-edge applications, including human healthcare, structural health monitoring, human-machine interfaces, and closed-loop device systems. However, crosstalk from multiple input signals severely deteriorates the sensing accuracy of the measured temperature and pressure. Moreover, different constituent materials and fabrication protocols utilized for flexible sensors hinder their integration towards

multifunctional e-skin. Here, this work introduces mechanically and electrically hybrid networks (MEHNs) in functional nanocomposites for large-area, multiplexed, and decoupled sensing. The rigid, high-resistive vanadium oxide (VO_2) microparticles with metal-insulator transition combined with soft, low-resistive liquid metal particles (LMPs) in MEHNs serve as temperature sensing units and mechanical buffers, respectively, leading to an ultra-high yet pressure-insensitive temperature coefficient of resistance (TCR) of -2.23%. Modifying VO_2 microparticles with silver nanoparticles to cancel the high TCR is combined with a porous structure to render the nanocomposite with temperature-insensitive pressure sensing with a sensitivity of 1.212% kPa^{-1}. The same constituent material and fabrication protocol of the MEHN nanocomposites, along with their scalability and recyclability, can afford low-cost, large-scale, and multiplexed e-skin for broad application opportunities, including human and battery health monitoring, soft electrical impedance tomography, and robotic perception.

Introduction

Human skin serves not only as a physical defensive system of the body against trauma but also as a key sensory system to perceive various external stimulations, including temperature[1, 2, 3], pressure[4, 5, 6, 7], and vibration[8, 9]. A skin-mimicking digital sensing system[10, 11, 12, 13, 14], i.e., the electronic skin (e-skin)[15, 16, 17], that combines high conformability and precise perception, is highly desired to address the formidable challenges in structural/physiological health monitoring[18, 19, 20], smart robotics[21, 22, 23], and prosthetic recovery[24]. In light of such practical demands, tremendous efforts and innovations in the design and fabrication of flexible pressure and temperature sensors, especially those based on resistive sensing, have been witnessed. Inspired by the unique texture of fingers for perception, various nanostructured or even hierarchically structured electrodes[25, 26, 27, 28, 29, 30] and porous separators[31, 32] have been successfully implemented to improve the electromechanical coupling of resistive-type pressure sensors for high sensitivity. Conventional flexible temperature sensors based on metallic patterns have a low temperature coefficient of resistance (TCR) and deformations can result in comparable resistance changes to temperature, leading to significant errors in temperature sensing. Although semiconducting materials have a high TCR, it is challenging to transfer semiconducting thin films to flexible substrates, and the resulting flexible temperature sensors are prone to mechanical failures. In contrast to pressure sensing, the electromechanical coupling of flexible temperature sensors needs to be suppressed to achieve accurate temperature measurements, which has become a longstanding bottleneck in this area. Alternatively, the thermoelectric effect of thin films, such as graphene[33, 34, 35], PEDOT:PSS[36, 37, 38], and carbon black[39, 40], has been exploited to address this challenge since their output voltage is insensitive to mechanical deformations. However, the millivolt-level output voltage of thermoelectric-based temperature sensors necessitates complex amplification circuits and off-sensor processing [1, 36], which is not favored for miniaturization and practical implementation.

Despite tremendous advances in flexible temperature and pressure sensing, their seamless integration to afford e-skin, like human skin, is still challenging due to the incompatibility between different constituent materials and fabrication processes employed.[41, 42, 43, 44, 45, 46, 47]. Placing temperature and pressure sensing units on the same plane for direct interfacing with objects to be measured is the most straightforward way to realize accurate dual-sensing, which, however, presents challenges for high-density integration. Moreover, temperature and pressure sensing were

not performed at the same spot with this design. Recently, vertical-stacking structures have been widely adopted in dual-sensing flexible devices to address this issue[48]. However, the design has several limitations: firstly, it requires compatible fabrication protocols for laminating the two sensing components; secondly, crosstalk between the sensing units and the increased overall thickness can significantly hinder its effectiveness in practical implementations. As mentioned above, leveraging the thermoelectric effect for temperature sensing can help to reduce crosstalk in vertical-stacking dual-sensing devices, but it requires complex circuiting and off-sensor processing. Moreover, to the best of our knowledge, scalable preparation of large-area sensing structures or materials to afford high-density, multiplex temperature and pressure mapping is still missing.

In this work, we introduce scalable preparation of functional nanocomposites for large-area, flexible, decoupled resistive dual-sensing e-skin. By introducing mechanically and electrically hybrid networks (MEHNs) consisting of rigid, metal-insulator transition material (i.e., VO_2 microparticles) and flowable, high-conductive liquid metal particles (LMPs), the flexible nanocomposite shows an ultra-high TCR and extraordinary pressure insensitivity. Modifying the VO_2 microparticle with silver nanoparticles to cancel out the high TCR, along with incorporated porous structures, endows the resulting nanocomposite with decoupled pressure sensing. The same constituent material and fabrication protocol used for pressure and temperature sensors allow vertical integration to afford ultra-thin, large-area, and multiplex e-skin. The pliable, large-area, and highly sensitive e-skin allows simple implementation in physiological conditions and battery health monitoring, as well as large-area temperature and pressure mapping, which can advance the development of human-machine interfaces and closed-loop robots.

Results

Design of the nanocomposite for decoupled temperature and pressure sensing.

Three key features of human skin are found to be responsible for the decoupled sensing capabilities, i.e., the vertical integration, similar constituent compositions (i.e., mainly collagen), and gradient structures[49]. Inspired by human skins, the flexible integrated e-skin with decoupled sensing capabilities consists of pressure-insensitive temperature (T) and temperature-insensitive pressure (P) sensing units based on the same yet judiciously formulated VO_2 microparticles and LMPs nanocomposite system (**Fig. 1a**). The key factor contributing to the decoupled dual-sensing of the nanocomposite system lies in sedimentation-induced MEHNs consisting of soft, low-resistive

LMPs and rigid, high-resistive VO_2 microparticles that are formed during thermoplastic polyurethane (TPU) curing (**Fig. 1b**). The fabrication of sensing nanocomposites is detailed in the experimental section and **Fig. S1**. To be specific, the VO_2 microparticle in the MEHN, a typical metal-insulator transition (MIT) material, can provide high temperature sensitivity of the T-unit, where optimized LMP loadings act as mechanical buffers to provide pressure-insensitivity (**Fig. 1c-i**). In the P-unit, the porous structure from phase separation results in a lower overall stiffness to improve pressure sensitivity, where the VO_2 microparticle is modified with Ag nanoparticles (**Fig. S2**) to give a vanishing temperature coefficient of resistance (TCR) (i.e., temperature insensitivity) (**Fig. 1c-ii**). One important aspect in preparing MEHNs is to avoid leakage or mechanical sintering of LMPs, which will exclude VO_2 microparticles from MEHNs and fail the temperature and pressure sensing of nanocomposites. Despite tremendous advances in flexible dual-sensing devices by previous literature reports, they are still severely restricted by either complex patterning of sensing materials or their mutual integration due to the incompatible constituent materials or fabrication process. The nanocomposite-based e-skin combines the figure-of-merits of a small thickness, scalable production, multiplex sensing, and even recycling by simply resolving and centrifuging. The same constituent material and resistivity sensing mechanism of the T-unit and P-unit enable high-density vertical integration and simple off-sensor processing, along with recyclability, compared to other dual-mode flexible sensors reported in previous studies[42, 44, 47, 48, 50, 51, 52] (**Fig. 1d**). The ultrathin, high-density, dual-sensing e-skin allows straightforward implementation on human bodies, devices, and robots, which can open up opportunities for human healthcare, battery health monitoring, robot perception, and human-machine interfaces (**Fig. 1e**).

Design and sensing performance of the T-unit

Tungsten-doped VO_2 microparticle is employed in the T-unit due to its significant resistance change from the metal-insulator transition (MIT) at room temperature (~ 311 K). To verify its temperature sensitivity, a thin film is prepared by hot-pressing tungsten-doped VO_2 microparticles. It exhibits a high TCR of -2.7% K^{-1} at the MIT temperature, which is one order higher than conventional metal-based resistive sensors (0.03-0.06% K^{-1}) and comparable to flexible temperature sensors based on epitaxial-growth semiconducting thin films[53] (**Fig. S3**). These results confirm the efficacy of the tungsten-doped VO_2 microparticles as the filler for temperature

sensing. However, due to the low aspect ratio of microparticles, the nanocomposites have a very high percolation threshold and are sensitive to deformations, i.e., the strong electromechanical coupling, which is a main bottleneck of flexible temperature sensors. The VO_2/TPU nanocomposite features a sedimentation-induced VO_2-rich layer with thickness determined by the VO_2 fraction (**Fig. S4**). The nanocomposite with a mixing ratio of 2.8: 1 (the weight ratio) shows an initial resistance of 12.6 MΩ at room temperature (i.e., 297 K), and it increases dramatically to giga-ohms with decreasing VO_2 fractions (**Fig. S5**), revealing a percolation threshold of ~ 2: 1 for W_{VO_2}: W_{TPU}. The resistance of the VO_2/TPU nanocomposite decreases dramatically upon compression, showing strong electromechanical coupling (**Fig. S6**). To mitigate this issue, we introduce a MEHN to the nanocomposite, combining rigid, high-resistive VO_2 microparticles and soft, low-resistive LMPs to serve as temperature sensing units and mechanical buffers, respectively (**Fig. 2a**). The VO_2 microparticle and the LMP prepared by tip sonication have a size of ~ 10 and 0.8 μm (**Fig. S7**). SEM images reveal the MEHN structure at the bottom of the VO_2/LMP/TPU nanocomposite, where LMP clusters are interlaced around VO_2 microparticles, forming point-to-surface contacts that effectively bridge VO_2 microparticles (**Fig. S8**). Compared with VO_2 microparticles, LMPs are more uniformly distributed throughout the film, while still exhibiting dense packing near the bottom, possibly due to interactions with VO_2 microparticles. The key to designing the nanocomposite-based T-unit lies in the relative ratio of VO_2 microparticles and LMPs in MEHNs. A low ratio of LMPs cannot effectively suppress the electromechanical coupling within the nanocomposite. Considering the large resistivity difference of VO_2 microparticles and LMPs, a high ratio of LMPs will lower the contribution of VO_2 microparticles in MEHNs and suppress the temperature sensitivity. On the other hand, the nanocomposite with bare LMPs (i.e., LMP/TPU) with a high loading (W_{LMP}: W_{TPU} = 2: 1, wt.%) is non-conductive because insulating barriers between spatially separated LMPs prevent the formation of percolative conductive networks, which is consistent with previous reports[54, 55, 56]. Uniaxial stretching of 50%, the nanocomposite remains non-conductive possibly due to the high yield stress of small-sized LMPs. However, leakage occurs in the LMP/TPU nanocomposite with further increased LMP loading (W_{LMP}: W_{TPU} = 5: 1, wt.%) after pressing (**Fig. S9**). These results reveal an abrupt transition of LMP-based nanocomposite from the non-conductive to conductive state with increasing LMP ratios and applied deformations. Most importantly, an LMP loading below its leakage threshold should be adopted to exploit the VO_2 microparticle in MEHNs for temperature

sensing. Without the loss of generosity, W_{LMP} = 2 is selected as the starting point for optimizing the nanocomposite for temperature sensing. Impressively, introducing a small amount of VO_2 microparticles (W_{VO_2} = 0.8, 1.4, 2.0) renders the non-conductive LMP/TPU nanocomposite conductive without mechanical activation, indicating the successful formation of MEHNs. XPS and DSC characterizations are carried out to elucidate the interaction between VO_2 and LMPs. XPS reveals the partial reduction of V^{4+} by inner Ga atoms through oxygen vacancy migration in the VO_2/LMP composites prepared by direct grinding and mixing (**Fig. S10**), which leads to a slight shift of the phase transition of VO_2 (**Fig. S11**). However, in the actual TPU-based nanocomposite, the contact between VO_2 microparticles and LMPs is spatially limited and physically constrained by the polymer matrix. As a result, such interfacial interactions are significantly suppressed and are therefore believed to have a negligible influence on the intrinsic phase transition behavior of VO_2 microparticles in the nanocomposite.

As expected, the initial resistance of the VO_2/LMP/TPU nanocomposite decreases with VO_2 loadings (**Fig. S12**). However, the pressure-insensitivity of the VO_2/LMP/TPU composite requires reduced VO_2 loadings (**Fig. 2b**), which also slightly reduces temperature sensitivity due to its vanishing contribution in MEHNs (**Fig. 2c**). For example, the TCR of the VO_2/LMP/TPU composite from 300 to 325 K decreases from -1.87% to -1.58% K^{-1} with W_{VO_2} decreasing from 2.8 to 0.8. Considering the aforementioned trade-off, the nanocomposite with W_{VO_2} of 0.8 (i.e., a mixing ratio of 0.8: 2: 1 for VO_2/LMP/TPU) is adopted for the T-unit, which exhibits a linear response (R^2=0.99) in the temperature range from 300 to 325 K. It is worth noting that the sensing curve of the T-unit is almost unaffected (<1%) as the applied pressure increases to 220 kPa (**Fig. 2d**). Besides the high precision to detect the small temperature change of 1 K (**Fig. 2e**), the T-unit also shows a consistent response to dynamic temperature cycles increased from 305 to 320 K (**Fig. 2f**). The consistent temperature sensing performance of the T-unit is also verified by the cyclic heating and cooling between 307 K and 300 K (**Fig. 2g**). It was also observed that reduced VO_2 loading also results in lower stiffness and higher compliance of the VO_2/LMP/TPU nanocomposite (**Fig. S13**).

For comparison, W_{LMP} = 1 and 3 are also selected as starting points in the optimization of the T-unit. It is found that the T-unit with a high LMP fraction (W_{LMP} = 3) suffers from pronounced leakage and particle sintering at the bottom, which ultimately disables the sensing capability of the

nanocomposite (**Fig. S14**). When the LMP fraction is reduced from W_{LMP} = 2 to W_{LMP} = 1, a higher VO_2 fraction (W_{VO_2}> 0.8) is required to render the nanocomposite electrically conductive. The T-unit with W_{LMP} = 1 also exhibits increasing temperature sensitivity and decreasing pressure sensitivity with increasing VO_2 fraction (**Fig. S15**), which is consistent with the trend observed for W_{LMP} = 2. These results further validate the proposed sensing mechanism based on MEHNs. Even though global optimization of the sensing performance is not the aim of this work, the VO_2/LMP/TPU nanocomposite with a weight ratio (W_{VO2}: W_{LMP}: W_{TPU}) of 1.0: 2.0: 1.0 exhibits effectively decoupled temperature sensing from pressure with a high TCR of −2.23 % K^{-1}. The results from this work compare favorably with the other flexible temperature sensors in previous literature reports, in terms of fabrication methods, sensitivity, and working range (**Table S1**).

Design and sensing performance of the P-unit

In the P-unit with the same constituent materials and MEHNs, introducing porous structures in the nanocomposite via phase separation results in a low mechanical stiffness (**Fig. S16**), which is crucial for improving its pressure sensitivity and working range[57, 58, 59]. The pressure-sensing capability of the nanocomposite relies on the dynamic change of MEHNs upon deformations (**Fig. 3a-i**), including the intercontact between VO_2 microparticles within TPU matrices and the contact between VO_2 microparticles and soft LMPs. The temperature sensitivity of the nanocomposite is suppressed by rationally modifying VO_2 microparticles (negative TCR) with silver nanoparticles (AgNPs) (positive TCR) for a vanishing TCR (**Fig. 3a-ii**). SEM and EDS images reveal the uniform distribution of VO_2 microparticles and LMPs on the pore wall (**Fig. S17)**. XPS characterization reveals the interactions between AgNP and VO_2 (**Fig. S10**). The Ag *3d* peak at ~368.2 eV in AgNP_VO_2 is consistent with that of pristine metallic Ag, while the V *2p* peak at ~530.0 eV corresponds to VO_2, suggesting that no strong chemical bonding between Ag and V atoms, either directly or mediated by oxygen, is formed. Notably, a slight shift of the V *2p* peak from 516.8 to 516.2 eV is observed after AgNP modification, indicating interfacial charge transfer at the AgNP/VO_2 interface. The negligible influence of AgNP modifications on the intrinsic electronic structure of VO_2 is further validated by its unchanged phase transition (**Fig. S11**). Instead, it is primarily attributed to the additional conductive pathways introduced by the AgNP coating. In this configuration, electrical current can flow not only through the VO_2 core but also along the AgNP-coated surface, which can further connect to the liquid metal particle network. The

coexistence of these parallel transport pathways effectively compensates for the high negative TCR of VO_2, resulting in the observed TCR cancellation. In comparison with the porous nanocomposite with MEHNs, the one with bare LMPs cannot afford pressure sensing since it either remains non-conductive (in the case of low LMP loadings) or undergoes an abrupt switch from the non-conductive to conductive state upon compression (in the case of high LMP loadings). Again, the relative ratio of VO_2 microparticles and LMPs in the porous nanocomposite needs to be optimized to cancel out their TCR for decoupled pressure sensing. As the LMP weight (W_{LMP}) increases from 3.3 to 8.3 (for W_{VO_2} = 3.3), the normalized relative resistance change of the nanocomposite decreases from 80% to 20% in the temperature range from 295 to 320 K (**Fig. 3b**). The decreasing response of the nanocomposite to temperature with LMP loadings indicates the increasing contribution of LMPs in MEHNs. Further increasing W_{LMP} to 10 switches the previously observed negative TCR to positive TCR, due to the formed conductive LM layer from the LMP sedimentation and leakage (**Fig. S18**). However, the 2D conductive network formed by LM cannot afford pressure sensing due to the limited change in conductive pathways upon deformation. Instead of elaborately optimizing LMP fractions, we turn to tuning the TCR of VO_2 microparticles via surface modifications. As coating VO_2 microparticles (negative TCR) with AgNPs (positive TCR) can further tune the TCR, increasing the Ag^+ precursor concentration increases the amount of AgNPs on VO_2 (**Fig. S19**), which also switches the TCR of the resulting nanocomposite (W_{LMP}: W_{VO2}: W_{TPU} = 8.3: 3.3: 1) from negative to positive (**Fig. 3c**). The TCR of <0.03% with the Ag^+ precursor of 60 mM provides temperature insensitivity for the P-unit, which is adopted in the following study unless specified otherwise. The porous nanocomposite with bare AgNP-modified VO_2 microparticles (AgNP_VO_2) is found to have a negligible resistive response to small compression, possibly due to the limited change of conductive pathways in the porous structure (**Fig. S20**). Although LMPs are a constituent of the hybrid conductive network, their contribution to the temperature sensitivity of the nanocomposite with a low LMP loading is negligible, particularly within the phase-transition temperature range of VO_2. This is because LMPs possess both a significantly lower resistance and a much smaller TCR compared to the abrupt and highly nonlinear resistance change associated with the MIT of VO_2. As a result, the temperature response of the nanocomposite is dominated by VO_2. It should be noted that such temperature-sensitivity cancellation is effective primarily within the phase-transition regime of VO_2, which will gradually

fail when VO_2 behaves as a pure semiconductor or a fully metallic phase outside this temperature range (~ 300-320 K).

Furthermore, other solid fillers with positive (iron microparticles) or negative (silicon oxide microparticles) TCR are introduced to the nanocomposite to test their efficacy in forming MEHNs for decoupled pressure sensitivity. With the same loading of fillers, the SiO_2/LMP/TPU nanocomposite fails to construct MEHNs for sensing, while the Fe/LMP/TPU nanocomposite shows a high resistive response to temperature (**Fig. S21**). Neither of these nanocomposites can afford pressure sensing with decoupled temperature interferences. All these results indicate that judiciously engineering the constituent fillers and their ratios in MEHNs is the key to realizing decoupled pressure sensing. *In-situ* SEM characterization reveals pore shrinkage of the nanocomposite under compression, which leads to densification and interconnection of conductive pathways along the pore walls (**Fig. S22**). As a result, the P-unit shows a nonlinear response to pressure, which can be approximated to be piecewise linear with a sensitivity of 1.21% (0-23 kPa), 0.28% (23-92 kPa), and 0.11% kPa^{-1} (92-220 kPa) (**Fig. 3d**). Meanwhile, the effect of temperature in the range from 298 to 318 K on the pressure-sensing performance of the P-unit is negligible, as evidenced by both the absolute and normalized resistance changes with increasing pressure (**Fig. 3e** and **Fig. S23**). Besides consistent response to different pressure loadings from 44 to 220 kPa (**Fig. 3f**), the P-unit also exhibits reliable sensing performance to 100 kPa over 100 cycles (**Fig. 3g**). To gain insight into the MEHN-based sensing, W_{VO_2} = 2.3 and 4.3 are also selected as the starting point in the optimization of the P-unit for comparison. The nanocomposite with W_{VO_2} = 2.3 remains non-conductive even with a high loading of LMPs until leakage appears (**Fig. S24**). With the VO_2 fraction increases to W_{VO_2} = 4.3, decreased temperature sensitivity is also observed in the nanocomposite with LMP loadings (**Fig. S25**). A low TCR of 0.1% is achieved for the nanocomposite with a weight ratio (W_{VO_2}: W_{LMP}: W_{TPU}) of 3.3: 10.3: 1.0, and further optimization can be performed via AgNP coating on VO_2 microparticles. Previous studies have demonstrated that the electromechanical coupling of stretchable sensors is strongly dependent on microstructures[60, 61, 62], and it is believed that the nonlinear response of porous sensing units typically originates from the limited deformation once the pores are fully collapsed. Although achieving a wide linear pressure-response range is beyond the scope of this work, the incorporation of hierarchical porous microstructures provides a promising strategy to extend the linear sensing

regime in future designs. A systematic investigation of pore-structure optimization and its influence on linearity will be pursued in future work.

Decoupled sensing performance of the integrated unit and array.

Together with patterned LMPs transfer printed from the glass (donor) to the TPU (receiving) substrate on both sides for stretchable interconnects with thin TPU passivation at the intersection (**Fig. S26**), the T-unit and P-unit in an array can be vertically integrated for decoupled sensing of temperature and pressure (**Fig. 4a**). Although both sensing units rely on resistive readout, electrical crosstalk within an integrated sensing unit is effectively avoided by introducing a double-sided electrode interlayer (with two independent electrode pairs). Almost unchanged sensing performance is observed in terms of response magnitude (**Fig. 4bc**) and rate (**Fig. 4de**) for both the T-unit (**Fig. 4bd**) and P-unit (**Fig. 4ce**), because fast heat transfer occurs in the T-unit stacked on the top and the stiffness difference between the two units allows strain localization in the P-unit. The signal-to-noise ratio (SNR) of the T-unit and P-unit in the integrated unit is evaluated by following a well-established method, defined as

$$\mathrm{SNR} = 20\log_{10}\left(\Delta R_{\mathrm{signal}}/\sigma_R\right) \quad (1)$$

where $\Delta R_{\mathrm{signal}}$ is the resistance change induced by thermal or pressure stimuli and σ_R is the resistance noise. Under stimuli of 1 K and 10 kPa, the T-unit and P-unit exhibit high SNR values of approximately 15 dB and 20 dB, respectively (**Fig. S27**). The integrated sensing unit can successfully detect the temperature without the pressure loading (from a hot gun), the pressure loading without the temperature stimulus (from a weight), and the simultaneous pressure and temperature stimuli (from a beaker with hot water) (**Fig. 4f**). Qualitatively measuring the response of the sensor under precisely controlled thermal and pressure stimuli applied by a 200 g weight equipped with a ceramic heater also rules out the transient coupling between the T-unit and P-unit (**Fig. S28**). The e-skin with an integrated 4×4 array can effectively map the thermal and pressure distribution (**Fig. 4g**). With room-temperature water filling the beaker, the P-unit array maps the pressure distribution, while the T-unit array shows negligible response due to the unchanged temperature. By filling an additional 60°C water, the P-unit array accurately maps the increasing pressure loaded by the beaker. Meanwhile, the T-unit array also shows the temperature distribution of the warm beaker as a result of filling warm water. The increasing pressure and decreasing

temperature caused by further filling the beaker with 8°C cold water are captured by the integrated e-skin. Electrical measurements of the sensor array with a pixel under thermal, pressure, and combined stimuli confirm negligible crosstalk between neighboring units, which can be attributed to the individual-addressable design (**Fig. S29**). A comprehensive comparison of the sensing performance of the dual-sensing interface in this work and previous literature reports (**Table S2**) highlights its simple off-sensor processing due to the same resistive sensing mechanism of the two sensors. It is worth noting that the raw materials (including TPU, VO_2 microparticles, and LMPs) of dual-sensing e-skin are ready to be recycled by two cycles of dissolving and centrifuging (**Fig. 4h**). Therefore, the reported nanocomposite-based sensors offer additional advantages of eco-friendliness and cost effectiveness.

Besides sensitivity, uniformity and long-term stability are critical metrics for evaluating sensor arrays. Since the MEHN is formed through the spontaneous sedimentation of LMPs and VO_2 microparticles during TPU curing, key parameters, including particle size, mixture viscosity, solvent evaporation rate, and curing conditions, are carefully controlled to ensure reproducible morphology and sensing performance. The viscosity of TPU precursors, film thickness (~200 μm), and curing environment are kept consistent across batches. Although nonuniformity in particle distribution is inevitable, the variation can be effectively averaged within a sensing area larger than 1 mm^2. For array fabrication, each sensing pixel is laser-cut from the central region of the nanocomposite film to avoid edge nonuniformity caused by the coffee-ring effect. As a result, the fabricated sensors exhibit low pixel-to-pixel variation for both temperature sensing (4.2% at 310 K) and pressure sensing (<3.6% at 44 kPa) (**Fig. S30**). The T-unit and P-unit also show low variation of 3.0% (at 310 K) and 2.9 % (at 44 kPa) across five batches. Moreover, both the T-unit and P-unit exhibit negligible changes in their sensing responses after 1,000 cycles of repetitive compression, confirming the excellent mechanical and electrical stability of the sensors (**Fig. S31**). These results rule out liquid metal leakage and AgNP detachment, as further confirmed by SEM characterizations of the nanocomposite (**Fig. S32**) and recycled AgNP_VO_2 (**Fig. S33**) after repetitive compression.

Applications of e-skin

The ultra-thin profile, flexibility, and high sensitivity of the integrated sensor e-skin enable conformal attachment to human skin for physiological conditions and movement monitoring. For instance, the e-skin can be attached to the wrist using a thin acrylic PU adhesive to monitor bending states via pressure detection (**Fig. 5a**). A large decrease in resistance from the P-unit indicates a higher degree of wrist bending. In another demonstration, the e-skin is utilized to monitor throat movements, offering the potential for early diagnosis and management of dysphagia. The subtle deformations caused by swallowing are detected by the P-unit with high sensitivity. As shown in **Fig. 5b**, saliva swallowing induces a resistance decrease of ~10% in the P-unit, demonstrating excellent sensitivity and repeatability. The highly responsive T-unit within the integrated sensor enables non-contact temperature monitoring. For example, when incorporated into a face mask, the sensor can accurately measure respiration rates (**Fig. 5c**). Since exhaled air is warmer than the ambient environment (~24°C), breath produces a noticeable decrease in the T-unit. Due to its high sensitivity and rapid response and recovery, the respiration rate recorded by the integrated sensor aligns closely with manual counting, ensuring precise and reliable respiration measurements.

The high sensitivity and low thickness of the integrated sensors facilitate their straightforward integration into devices for structural and health monitoring applications. Overheating during high-power charging or discharging is a well-known cause of battery failure and safety concerns. To demonstrate the utility of the integrated sensor, it is attached to the surface of lithium-ion pouch cells to monitor temperature and pressure changes in real-time during charging and discharging cycles (**Fig. 5d**). After attaching the integrated sensor, the pouch cell is clamped by two acrylic plates to imitate actual working conditions of battery packs. The lithium-ion pouch cell, with a 2 Ah capacity, is subjected to constant current (CC) charging at a current density of 1 C until reaching a cutoff voltage of 4.2 V, followed by constant voltage (CV) charging at 4.2 V until the current dropped to 0.005 C. Subsequently, the cell undergoes CC discharging at a current density of 1 C with a cutoff voltage of 3 V. During the CC charging phase, lithium ions are deintercalated from the cathode and intercalated into the anode, leading to volumetric expansion of the anode and an increase in internal pressure. Concurrently, electrochemical reactions and charge transfer generate heat to result in a temperature rise. The T-unit and P-unit of the integrated sensor effectively detect the temperature and pressure increases. During the CV charging phase, the internal pressure decreases as the current diminishes, as evidenced by the increased resistance of

the P-unit. The reduced charging current leads to slower heat generation, which is reflected in the increased resistance of the T-unit. In the CC discharging phase, lithium ions are deintercalated from the anode and intercalated into the cathode, causing anode contraction and a reduction in internal pressure. However, the high discharging current generates significant heat, resulting in a temperature rise, as recorded by the T-unit. Notably, the T-unit demonstrates temperature sensing performance comparable to that of commercial thermistors (**Fig. S34**), with additional advantages such as low cost and ease of implementation. These findings confirm the efficacy of the integrated sensor for real-time and continuous monitoring of batteries, offering valuable support for advanced battery management systems and safety assurance.

The functional nanocomposite can be produced with a low thickness and on a large scale, making it highly suitable for temperature and pressure mapping applications on curvy surfaces. Of note, an entire nanocomposite sheet without being patterned into units can afford multiplex temperature and pressure sensing, which can avoid the alignment issue for reduced fabrication complexity. As shown in **Fig. 5e-i**, an ultrathin, multiplex (8×4) e-skin can be conformally attached to human fingertips and arms. As another example, a large-size, 3×3 dual-sensing e-skin is integrated with fabrics or clothing through hot pressing and can ensure conformal contact with human tissue, even at highly mobile joints such as the shoulder and elbow (**Fig. 5e-ii**). Crosstalk between sensing pixels can be effectively suppressed as long as the interelectrode distance within each pixel is smaller than the distance between adjacent pixels. Importantly, the e-skin integrated into fabrics maintains consistent temperature and pressure sensing performance in the wearable form.

Electrical impedance tomography (EIT) offers high-density mapping capabilities without the limitations imposed by electrode structures in conventional mapping techniques. A dual-sensing EIT e-skin enables precise simultaneous mapping of temperature and pressure. The high uniformity of sensing sheets is one of the key factors that ensure accurate mapping. A 64×64 mesh corresponding to 3216 pixels in the disk-shaped sensing area is exploited for image reconstruction. As demonstrated in **Fig. 5f**, the EIT interface adopting 16 peripheral electrodes is capable of differentiating single- and two-point pressure probing from glass bars. Additionally, the temperature distribution generated by a heat gun at random locations is effectively captured by the e-skin-based EIT interface. The EIT e-skin interface demonstrates high resolution with an effective pixel/interconnect ratio of ~210. The spatial resolution of the EIT-based e-skin is

estimated to be approximately 20% of the sensor diameter, as quantified by the full width at half maximum (FWHM) of reconstructed conductivity profiles. This resolution is comparable to that of conventional EIT systems employing a similar number of boundary electrodes[63, 64]. We note that a one-step reconstruction algorithm (i.e., NOSER[65]) is employed in this work, and thus, the spatial resolution is not expected to surpass that of state-of-the-art EIT systems. Nevertheless, with 16 boundary electrodes, the EIT reconstruction yields a much denser spatial map than a conventional 4 × 4 array sensor using the same number of electrodes. To the best of our knowledge, this work represents the first demonstration of a dual-parameter (temperature and pressure) EIT-based sensing interface. Further improvements in spatial resolution through optimized sensor design and advanced reconstruction algorithms will be pursued in future studies. It is believed that the large-scale production of the nanocomposite film, seamless integration with stretchable electrodes, and free-form laser patterning may pave the way towards customized EIT-based health monitoring or human-machine devices.

The e-skin enables robots to perceive both temperature and pressure, facilitating closed-loop systems. As a demonstration, a 1×3 dual-sensing array is integrated into a flexible gripper actuated by a motion stage (**Fig. 5g-i**). The pressure distribution along the gripper, measured by the P-unit, provides valuable information about the shape and material of objects (**Fig. 5g-ii**). For instance, a cubic object produces a more uniform pressure distribution compared to objects with curved surfaces, such as a ball or a cylinder. This difference arises from the gripper's limited ability to conform to curved surfaces. Additionally, softer and lighter objects correspond to a lower threshold pressure required for holding. For example, among objects of the same shape, the threshold pressure for holding a tissue pack is significantly lower than that for a foam piece or a 3D-printed Teflon object, which requires progressively higher pressures. The temperature-sensing capabilities of the T-unit further enhance the e-skin's functionality by providing additional data about objects. For example, when the gripper holds a beaker filled with either cold or hot water, the P-unit registers similar pressure distributions. However, the three T-units respond distinctly to hot water by exhibiting a significant reduction in resistance. The dual-sensing capabilities of the e-skin are believed to greatly enhance the utility of soft robots in challenging environments, advancing the development of robust closed-loop systems.

Discussion

This work introduces judicious design and preparation of functional flexible nanocomposites with LMPs and VO_2 microparticles as the filler to decouple temperature and pressure sensing. By exploiting the MIT of VO_2 and building MEHNs within the nanocomposite, the T-unit shows pressure insensitivity and an ultra-high TCR. The P-unit is prepared from the same constituent materials except Ag nanoparticle modifications on VO_2 microparticles to suppress temperature sensitivity. The same constituent material and fabrication of the T-unit and P-unit facilitate seamless, vertical integrations toward functional e-skin for high-density mapping. Of note, the constituent materials can be easily recycled by dissolving and centrifuging processes. The ultra-thin profile and high sensitivity of the nanocomposite-based e-skin allow its simple implementations in human movements, physiological conditions, and device/structure monitoring. Owing to the large-scale preparation and dense integration, the e-skin can afford temperature and pressure mapping through multiplex or EIT structures, which can advance the development of human-machine interfaces and closed-loop robots.

Methods

Materials

TPU and eutectic gallium–indium alloy (EGaIn, $Ga_{75.5}In_{24.5}$) were purchased from Chengdu Ega new material Co. LTD. Tungsten-doped VO_2 microparticles with a size of ~ 200 nm were supplied by Nangong City Kona new material technology Co. LTD. N, N-Dimethylformamide (DMF) (AR, 99.5%), 1-butanol (Anhydrous, 99.8%), tetrahydrofuran (THF) (AR, 99.0%), ammonia water (GR, 25-28%), and dopamine hydrochloride were purchased from Shanghai Aladdin Biochemical Technology Co. Ltd. Deionized (DI) water was prepared by a laboratory instrument (UPTA 20, Ultrapure water machine). All reagents were used without further purification.

Preparation of the nanocomposite for the T-unit

1.8 g EGaIn was added to a beaker with 30 mL DMF and tip-sonicated for 20 minutes in an ice bath. The obtained LMPs has an average diameter of 1 μm. The mixed solution containing LMPs was centrifuged at 3435 x g for 5 minutes to collect the LMPs from the bottom of the beaker. 720 mg TPU was dissolved in the 6 mL DMF solution at 60°C to form a pellucid solution. Next, 1.5 g EGaIn LMPs and VO_2 microparticles of different amounts were added into the solution, followed by mixing in a planetary mixer and degassing in a vacuum to remove air bubbles. The mixed solution was cured in a mold at 120°C for 1 hour to form the nanocomposite as the T-unit.

Preparation of the nanocomposite for the P-unit

VO_2 microparticles were first modified by polydopamine on the surface. Briefly, 1 g VO_2 microparticles were dispersed in the Tris-HCl buffer (500 mL, 1 mM) by ultrasound for 5 min to form a dark solution. After adding and fully mixing dopamine hydrochloride (500 mg) in the solution with a magnetic stirrer for 4 hours at room temperature, the VO_2 microparticles were collected and rinsed with DI water and ethanol alternatively three times, followed by drying at 60°C for 8 h. Following polydopamine modifications, Ag nanoparticles were modified on the surface of VO_2 by a simple reduction process. In brief, after dissolving silver nitrate in the DI water, the ammonia solution was added with different mixing ratios to obtain Ag^+ precursors with various concentrations. The dopamine-modified VO_2 microparticles (1 g), D-glucose, and Ag^+ precursor were mixed by a magnetic stirrer and allowed to react for 30 min. Finally, the collected AgNP_VO_2 microparticles were rinsed with the DI water and ethanol alternatively three times and then dried at 60°C for 8h. Meanwhile, TPU powders were dissolved in THF with a concentration of 70 mg/mL. EGaIn was added to the 1-butanol solution and then sonicated by a bath sonicator for 10 minutes. Next, the LMP dispersion with different loadings and AgNP_VO_2 microparticles was added to the TPU solution with a mixing volume ratio of 5:4 (1-butanal: THF). The fraction of AgNP_VO_2 microparticles and LMPs was optimized to provide temperature insensitivity. The mixture was then cured in a hood with well-controlled temperature, humidity, and airflow to obtain the nanocomposite as the P-unit. The thickness of the T-unit and P-unit was fixed to 200 μm for consistency.

Preparation of the dual-sensing e-skin

2g EGaIn was sonicated in the isopropyl alcohol solution (20 mL) for 40 minutes to obtain the LMP dispersion, which was air-sprayed onto a glass slice through a laser-patterned polyimide (PI) mask. A thin TPU sheet was prepared by spin-coating TPU precursor (70 mg/mL in DMF) on glass substrates, followed by degassing and curing at 120°C for 1 hour. Stretchable LM interconnects were fabricated by laminating the thin TPU layer on the LMP patterns, followed by manually pressing and peeling off. After gentle hot-pressing of the sensing units (i.e., T-unit and P-unit) into the LM-based interconnect, another TPU film was applied for encapsulation. In the fabrication of the integrated sensing unit, the LMPs were transferred to both sides of the TPU film

and then stacked with the T-unit and P-unit in a vertical configuration by gentle hot-pressing. In the case of dual-sensing arrays, LM-based electrical interconnects were fabricated by two separate transfer printing processes for the row and column patterns, with grid intersections insulated by TPU.

Mechanical, electrical, and structural measurement

The compressive stiffness of nanocomposites was characterized by a universal material testing machine (M230 Pro, Testing machine measurement and control system) at a rate of 1 N/s. The temperature control was provided by a Dewar tank equipped with a temperature controller (Model 325, Lake Shore), whereas the pressure was applied by a universal material testing machine. The resistance was measured in real-time with a multichannel digital multimeter (Keysight 2902). The sensitivity of the pressure sensor was calculated as the ratio of the normalized relative resistance change to the pressure change. Scanning electron microscopy (SEM) images taken from ZEISS (GeminiSEM 300) were used to characterize the morphology and elemental distribution of the samples.

Battery health monitoring

After attaching the dual-mode sensor to the surface of the in-house fabricated pouch cell (capacity of 2 Ah) with a PI tape, the positive and negative terminals of the pouch cell were connected to a battery testing device (CT-4008-5V20A-A, Shenzhen Neware Electronics Co., Ltd.), controlled by the BTS8.0 client software. The battery was charged using a constant current-constant voltage (CC-CV) method: the initial charging at CC till reaching a voltage of 4.2 V was followed by CV charging at 4.2 V till reaching a current of 0.05 C. Next, the battery was discharged at CC, with the cutoff voltage set at 3 V. The sensor outputs were recorded during the charging-discharging process.

Integration and demonstration of the smart soft gripper

A 1×3 dual-mode pressure/temperature sensor array was attached to one side of a flexible gripper (2 cm × 5 cm), which was electrically controlled to catch and release objects of various shapes and hardnesses. The shapes included a cube with a side of 4 cm, a cylinder with a base diameter of 4 cm and height of 4 cm, and a sphere with a diameter of 4 cm. Varying stiffnesses were provided by a resin cuboid, sponge, and paper tissue package.

Experiments on human subjects

All human subject studies were approved by The Pennsylvania State University (protocol number STUDY00020880) with the informed consent obtained from the volunteers.

Data Availability

The data generated in this study are provided in the Source Data file. Source data are provided with this paper. All data are available from the corresponding author upon request.

References:

1. Liu L*, et al.* Recent Advances in Flexible Temperature Sensors: Materials, Mechanism, Fabrication, and Applications. *Advanced Science* **11**, 2405003 (2024).

2. Zhang X*, et al.* Flexible Temperature Sensor with High Reproducibility and Wireless Closed-Loop System for Decoupled Multimodal Health Monitoring and Personalized Thermoregulation. *Advanced Materials* **36**, 2407859 (2024).

3. Liu Z*, et al.* A thin-film temperature sensor based on a flexible electrode and substrate. *Microsystems & Nanoengineering* **7**, 42 (2021).

4. Xu Z*, et al.* A flexible pressure sensor with highly customizable sensitivity and linearity via positive design of microhierarchical structures with a hyperelastic model. *Microsystems & Nanoengineering* **9**, 5 (2023).

5. Jiang T, Wang C, Ling T, Sun S, Yang L. Recent advances and new frontier of flexible pressure sensors: Structure engineering, performances and applications. *Materials Today Physics* **48**, 101576 (2024).

6. Xu C*, et al.* Flexible Pressure Sensors in Human–Machine Interface Applications. *Small* **20**, 2306655 (2024).

7. Wang X, Yu J, Cui Y, Li W. Research progress of flexible wearable pressure sensors. *Sensors and Actuators A: Physical* **330**, 112838 (2021).

8. Liu Y-F*, et al.* Spider-Inspired Ultrasensitive Flexible Vibration Sensor for Multifunctional Sensing. *ACS Applied Materials & Interfaces* **12**, 30871-30881 (2020).

9. Chen X*, et al.* Bio-inspired flexible vibration visualization sensor based on piezo-electrochromic effect. *Journal of Materiomics* **6**, 643-650 (2020).

10. Zarei M, Jeong AW, Lee SG. Whisker-Implanted Biomimetic Electronic Skin for Tactile Sensing and Blind Perception. *Advanced Science* **n/a**, 2408162 (2024).

11. Chun S*, et al.* An artificial neural tactile sensing system. *Nature Electronics* **4**, 429-438 (2021).

12. Gao H, Cai W, Li A, Du Y, Zhu J-L, Ye Z. Ultrasensitive Biomimetic Skin with Multimodal and Photoelectric Dual-Signal Sensing. *ACS Applied Materials & Interfaces* **16**, 21073-21083 (2024).

13. Zhou Q*, et al.* A Flexible Smart Healthcare Platform Conjugated with Artificial Epidermis Assembled by Three-Dimensionally Conductive MOF Network for Gas and Pressure Sensing. *Nano-Micro Letters* **17**, 50 (2024).

14. Guo X, Sun Z, Zhu Y, Lee C. Zero-Biased Bionic Fingertip E-Skin with Multimodal Tactile Perception and Artificial Intelligence for Augmented Touch Awareness. *Advanced Materials* **36**, 2406778 (2024).

15. Yang JC, Mun J, Kwon SY, Park S, Bao Z, Park S. Electronic Skin: Recent Progress and Future Prospects for Skin-Attachable Devices for Health Monitoring, Robotics, and Prosthetics. *Advanced Materials* **31**, 1904765 (2019).

16. Chen L*, et al.* Flexible and Transparent Electronic Skin Sensor with Sensing Capabilities for Pressure, Temperature, and Humidity. *ACS Applied Materials & Interfaces* **15**, 24923-24932 (2023).

17. Liu Y*, et al.* Electronic skin as wireless human-machine interfaces for robotic VR. *Science Advances* **8**, eabl6700.

18. Yang X*, et al.* Electronic Skin for Health Monitoring Systems: Properties, Functions, and Applications. *Advanced Materials* **36**, 2402542 (2024).

19. Cheng M*, et al.* A review of flexible force sensors for human health monitoring. *Journal of Advanced Research* **26**, 53-68 (2020).

20. Yao S, Swetha P, Zhu Y. Nanomaterial-Enabled Wearable Sensors for Healthcare. *Advanced Healthcare Materials* **7**, 1700889 (2018).

21. Zhao Z*, et al.* Large-Scale Integrated Flexible Tactile Sensor Array for Sensitive Smart Robotic Touch. *ACS Nano* **16**, 16784-16795 (2022).

22. Luo Z, Cheng W, Zhao T, Xiang N. Intelligent sensory systems toward soft robotics. *Applied Materials Today* **37**, 102122 (2024).

23. Sun T*, et al.* Artificial Intelligence Meets Flexible Sensors: Emerging Smart Flexible Sensing Systems Driven by Machine Learning and Artificial Synapses. *Nano-Micro Letters* **16**, 14 (2023).

24. Raspopovic S, Valle G, Petrini FM. Sensory feedback for limb prostheses in amputees. *Nature Materials* **20**, 925-939 (2021).

25. Zhang Y*, et al.* Highly stable flexible pressure sensors with a quasi-homogeneous composition and interlinked interfaces. *Nature Communications* **13**, 1317 (2022).

26. Tee BCK, Chortos A, Dunn RR, Schwartz G, Eason E, Bao Z. Tunable Flexible Pressure Sensors using Microstructured Elastomer Geometries for Intuitive Electronics. *Advanced Functional Materials* **24**, 5427-5434 (2014).

27. Chou H-H*, et al.* A chameleon-inspired stretchable electronic skin with interactive colour changing controlled by tactile sensing. *Nature Communications* **6**, 8011 (2015).

28. Ha M, Lim S, Park J, Um D-S, Lee Y, Ko H. Bioinspired Interlocked and Hierarchical Design of ZnO Nanowire Arrays for Static and Dynamic Pressure-Sensitive Electronic Skins. *Advanced Functional Materials* **25**, 2841-2849 (2015).

29. Wang Z, Zhang L, Liu J, Jiang H, Li C. Flexible hemispheric microarrays of highly pressure-sensitive sensors based on breath figure method. *Nanoscale* **10**, 10691-10698 (2018).

30. Bae GY*, et al.* Pressure/Temperature Sensing Bimodal Electronic Skin with Stimulus Discriminability and Linear Sensitivity. *Advanced Materials* **30**, 1803388 (2018).

31. Kwon D*, et al.* Highly Sensitive, Flexible, and Wearable Pressure Sensor Based on a Giant Piezocapacitive Effect of Three-Dimensional Microporous Elastomeric Dielectric Layer. *ACS Applied Materials & Interfaces* **8**, 16922-16931 (2016).

32. Kim J-O*, et al.* Highly Ordered 3D Microstructure-Based Electronic Skin Capable of Differentiating Pressure, Temperature, and Proximity. *ACS Applied Materials & Interfaces* **11**, 1503-1511 (2019).

33. Descent P, Izquierdo R, Fayomi C. Printing of temperature and humidity sensors on flexible substrates for biomedical applications. In: *2018 IEEE International Symposium on Circuits and Systems (ISCAS)*) (2018).

34. Gu JF*, et al.* Multifunctional Poly(vinyl alcohol) Nanocomposite Organohydrogel for Flexible Strain and Temperature Sensor. *Acs Applied Materials & Interfaces* **12**, 40815-40827 (2020).

35. Han RG*, et al.* Facile fabrication of rGO/LIG-based temperature sensor with high sensitivity. *Mater Lett* **304**, 4 (2021).

36. Zhang F, Zang Y, Huang D, Di C-a, Zhu D. Flexible and self-powered temperature–pressure dual-parameter sensors using microstructure-frame-supported organic thermoelectric materials. *Nature Communications* **6**, 8356 (2015).

37. Isoniemi T, Tuukkanen S, Cameron DC, Simonen J, Toppari JJ. Measuring optical anisotropy in poly(3,4-ethylene dioxythiophene):poly(styrene sulfonate) films with added graphene. *Organic Electronics* **25**, 317-323 (2015).

38. Yu YY, Peng SH, Blanloeuil P, Wu SY, Wang CH. Wearable Temperature Sensors with Enhanced Sensitivity by Engineering Microcrack Morphology in PEDOT:PSS-PDMS Sensors. *Acs Applied Materials & Interfaces* **12**, 36578-36588 (2020).

39. Xu X-B, Li Z-M, Dai K, Yang M-B. Anomalous attenuation of the positive temperature coefficient of resistivity in a carbon-black-filled polymer composite with electrically conductive in situ microfibrils. *Applied Physics Letters* **89**, (2006).

40. Liu H*, et al.* A Flexible Multimodal Sensor That Detects Strain, Humidity, Temperature, and Pressure with Carbon Black and Reduced Graphene Oxide Hierarchical Composite on Paper. *ACS Applied Materials & Interfaces* **11**, 40613-40619 (2019).

41. Chen J*, et al.* Skin-Inspired Bimodal Receptors for Object Recognition and Temperature Sensing Simulation. *Advanced Functional Materials*, (2024).

42. Gao F-L*, et al.* Ti3C2Tx MXene-Based Multifunctional Tactile Sensors for Precisely Detecting and Distinguishing Temperature and Pressure Stimuli. *ACS Nano* **17**, 16036-16047 (2023).

43. Gao F-L*, et al.* Integrated temperature and pressure dual-mode sensors based on elastic PDMS foams decorated with thermoelectric PEDOT:PSS and carbon nanotubes for human energy harvesting and electronic-skin. *Journal of Materials Chemistry A* **10**, 18256-18266 (2022).

44. Ge C*, et al.* Dual-Function Tactile Sensor with Linear Pressure and Temperature Perception at Low Degree of Coupling. *Advanced Intelligent Systems* **5**, (2023).

45. Pang Z, Zhao Y, Luo N, Chen D, Chen M. Flexible pressure and temperature dual-mode sensor based on buckling carbon nanofibers for respiration pattern recognition. *Scientific Reports* **12**, (2022).

46. Wang C, Xia K, Zhang M, Jian M, Zhang Y. An All-Silk-Derived Dual-Mode E-skin for Simultaneous Temperature-Pressure Detection. *ACS Appl Mater Interfaces* **9**, 39484-39492 (2017).

47. Cai M, Jiao ZD, Nie S, Wang CJ, Zou J, Song JZ. A multifunctional electronic skin based on patterned metal films for tactile sensing with a broad linear response range. *Sci Adv* **7**, 10 (2021).

48. Duan S*, et al.* Bioinspired Young's Modulus-Hierarchical E-Skin with Decoupling Multimodality and Neuromorphic Encoding Outputs to Biosystems. *Advanced Science*, (2023).

49. Boer M, Duchnik E, Maleszka R, Marchlewicz M. Structural and biophysical characteristics of human skin in maintaining proper epidermal barrier function. *Postepy Dermatologii I Alergologii* **33**, 1-5 (2016).

50. Hong Q*, et al.* 3D dual-mode tactile sensor with decoupled temperature and pressure sensing: Toward biological skins for wearable devices and smart robotics. *Sens Actuator B-Chem* **404**, 11 (2024).

51. Wang JC*, et al.* Integrating In-Plane Thermoelectricity and Out-Plane Piezoresistivity for Fully Decoupled Temperature-Pressure Sensing. *Small* **20**, 10 (2024).

52. Yuan TK, Yin RL, Li CW, Wang C, Fan Z, Pan LJ. Fully inkjet-printed dual-mode sensor for simultaneous pressure and temperature sensing with high decoupling. *Chem Eng J* **473**, 13 (2023).

53. Liao F*, et al.* Ultrasensitive Flexible Temperature-Mechanical Dual-Parameter Sensor Based on Vanadium Dioxide Films. *IEEE Electron Device Letters* **38**, 1128-1131 (2017).

54. Fassler A, Majidi C. Liquid-Phase Metal Inclusions for a Conductive Polymer Composite. *Advanced Materials* **27**, 1928-1932 (2015).

55. Pan C*, et al.* A Liquid-Metal–Elastomer Nanocomposite for Stretchable Dielectric Materials. *Advanced Materials* **31**, 1900663 (2019).

56. Saborio MG*, et al.* Liquid Metal Droplet and Graphene Co-Fillers for Electrically Conductive Flexible Composites. *Small* **16**, 1903753 (2020).

57. Zhao X*, et al.* Flexible pressure sensor based on CNTs/CB/PDMS sponge with porous and microdome structures for sitting posture discrimination. *Chem Eng J* **502**, 157878 (2024).

58. Zeng P, Pan P, He J, Yang Z, Song H, Zhang J. Porous Composite PDMS for a Pressure Sensor with a Wide Linear Range. *ACS Applied Nano Materials* **7**, 455-465 (2024).

59. Zhang J*, et al.* Porous nanocomposites with enhanced intrinsic piezoresistive sensitivity for bioinspired multimodal tactile sensors. *Microsystems & Nanoengineering* **10**, 19 (2024).

60. Li Y*, et al.* Linear Range Enhancement in Flexible Piezoresistive Sensors Enabled by Double-Layer Corrugated Structure. *Advanced Functional Materials* **n/a**, e13480 (2025).

61. Wu L*, et al.* Beetle-Inspired Gradient Slant Structures for Capacitive Pressure Sensor with a Broad Linear Response Range. *Advanced Functional Materials* **34**, 2312370 (2024).

62. Yang R*, et al.* Iontronic pressure sensor with high sensitivity over ultra-broad linear range enabled by laser-induced gradient micro-pyramids. *Nature Communications* **14**, 2907 (2023).

63. Djajaputra D. Electrical Impedance Tomography: Methods, History and Applications. *Medical Physics* **32**, 2731-2731 (2005).

64. Duan X, Taurand S, Soleimani M. Artificial skin through super-sensing method and electrical impedance data from conductive fabric with aid of deep learning. *Scientific Reports* **9**, 8831 (2019).

65. Cheney M, Isaacson D, Newell JC, Simske S, Goble J. NOSER: An algorithm for solving the inverse conductivity problem. *International Journal of Imaging Systems and Technology* **2**, 66-75 (1990).

Acknowledgments

This work is supported by the Natural Science Foundation of China under grant Nos. 62427806, 62301116, and the Fundamental and Interdisciplinary Disciplines Breakthrough Plan of the Ministry of Education of China under grant No. JYB2025XDXM406. H.C. acknowledges the support provided by NIH (Award No. R21EB030140), NSF (Grant Nos. 2309323, 2243979, 2319139, and 2222654), and Penn State University.

Author Contributions

J.Z., H.C., and J.L. conceptualized the study. J.Z., Y.C., H.L., Y.H.C., J.Y., H.C., and Y.L. developed the methodology. X.L., J.L., and Y.Q. performed the primary experiments and conducted data analysis and curation. Y.X. and X.M. assisted with the experiments. J.Z., Y.C., H.L., H.C., and Y.L. drafted the manuscript. Z.H., M.G., T.P., J.Y., H.C., and Y.L. reviewed the manuscript and provided critical revisions. J.Z. and Y.L. acquired funding and supervised the project. All authors discussed the results and approved the final version of the manuscript.

Competing Interests

The authors declare no competing interests.

Figure Legends/Captions (for main text figures)

Fig. 1. Schematics showing the bio-inspired e-skin with decoupled temperature and pressure sensing. (a) Schematics showing key features of human skin and bio-inspired integrated sensors. **(b)** Design strategies of the mechanically and electrically hybrid network (MEHN) in nanocomposites for decoupled dual sensing of temperature and pressure. **(c)** Schematics illustrating the nanocomposite for temperature (i.e., the T-unit) and pressure (i.e., the P-unit) sensing. **(d)** Radar plot showing the performance comparison between the nanocomposite-based e-skin from this work and the others in the literature reports.[42, 44, 47, 48, 50, 51, 52] **(e)** Applications of nanocomposite-based e-skin in physiological condition and battery health monitoring, human-machine interfaces, and soft robotics.

Fig. 2. Sensing mechanism and performance of the T-unit. (a) (i) Schematics showing the sensing mechanism of the nanocomposite with single (SCNs) or mechanically and electrically hybrid networks (MEHNs). **(ii)** Schematics showing the optimized VO_2 fractions for decoupled temperature and pressure sensing. **(b)** Measured electromechanical response and **(c)** temperature sensing performance of the nanocomposite with varied VO_2 fractions. **(d)** Temperature sensing performance of the optimized VO_2/LMP/TPU nanocomposite (i.e., the T-unit) at different

pressures. **(e)** Resistive response of the T-unit under a temperature gradient of 1 K. **(f)** Resistive response of the T-unit under dynamic cycling of different temperatures. **(g)** Resistance response of the T-unit under the cyclic temperature change between 300 and 307 K.

Fig. 3. Sensing mechanism and performance of the P-unit. **(a) (i)** Schematics showing the sensing mechanism of the porous nanocomposite P-unit. **(ii)** Schematics showing the incorporation of Ag nanoparticles (AgNPs, positive TCR) on VO_2 microparticles (negative TCR) to achieve zero TCR. Measured resistive response of the porous nanocomposite with varied **(b)** LMP fractions and **(c)** Ag nanoparticle modifications to the increasing temperature. **(d)** Pressure sensing performance of the porous nanocomposite with optimized LMP fractions and AgNP modifications (i.e., the P-unit). **(e)** Pressure sensing performance of the P-unit at different temperatures. **(f)** Resistive response of the P-unit under dynamic cycling of different pressure loads. (g) Resistive response of the P-unit under cyclic pressure loads of 100 kPa (1,000 times).

Fig. 4 Decoupled sensing performance of the vertically integrated e-skin. **(a)** Optical images of the integrated e-skin with the single-unit or array configuration. **(b)** Temperature and **(c)** pressure sensing performance of the T-unit and P-unit before and after integration. Response time of the **(d)** T-unit and **(e)** P-unit before and after integrations. **(f)** Sensing performance of the integrated e-skin unit upon thermal or pressure stimuli by a hot gun, a weight, and a beaker containing hot water. **(g)** Pressure and temperature mapping by the e-skin with different stimuli, including a beaker with cold water, followed by filling with hot and cold water subsequently. **(h)** Recyclability of LM and VO_2 in the e-skin by simple dissolving and centrifuging.

Fig. 5 Demonstration of the e-skin in physiological condition and battery health monitoring, electrical impedance tomography (EIT), on-body sensing, and machine perception. Monitoring of **(a)** wrist movement, **(b)** swallowing, and **(c)** respiration by the integrated e-skin. **(d)** Attaching the integrated sensor to a lithium-ion pouch cell for battery health monitoring upon charging and discharging cycles. **(e)** Integrating the e-skin with fabrics for on-body sensing. **(i)** Optical images of a thin, multiplex (4×8), dual-sensing e-skin attached conformally on human fingertips and arms, and the integrated e-skin on fabrics. **(ii)** Optical images of a large-size dual-sensing e-skin integrated on fabrics and its sensing performance in the free-standing state or being integrated into fabrics. **(f)** A dual-sensing EIT interface for mapping the one- or two-point pressing and thermal stimulation by a hot gun. **(g)** The integrated e-skin endows soft robotics with perceptive capabilities. **(i)** Optical images of soft grippers with integrated e-skin. **(ii)** Temperature and pressure mapping when using the gripper to grab objects with different shapes (i.e., cube, cylinder, and sphere), different temperatures (i.e., a beaker containing cold or hot water), or made of different materials (i.e., Teflon, foam, and tissue paper pack). Grabbing and releasing cycles are repeated three times.

Editorial summary: Electronic skins are capable to monitor stimuli such as temperature and pressure, though they are susceptible to crosstalk diminishing sensitivity. Here the authors report a mechanically and electronically hybrid network using vanadium oxide and liquid metal particles to optimize selectivity and sensitivity.

Peer review information: *Nature Communications* thanks Bin Hu and Zheng Yan for their contribution to the peer review of this work. A peer review file is available.

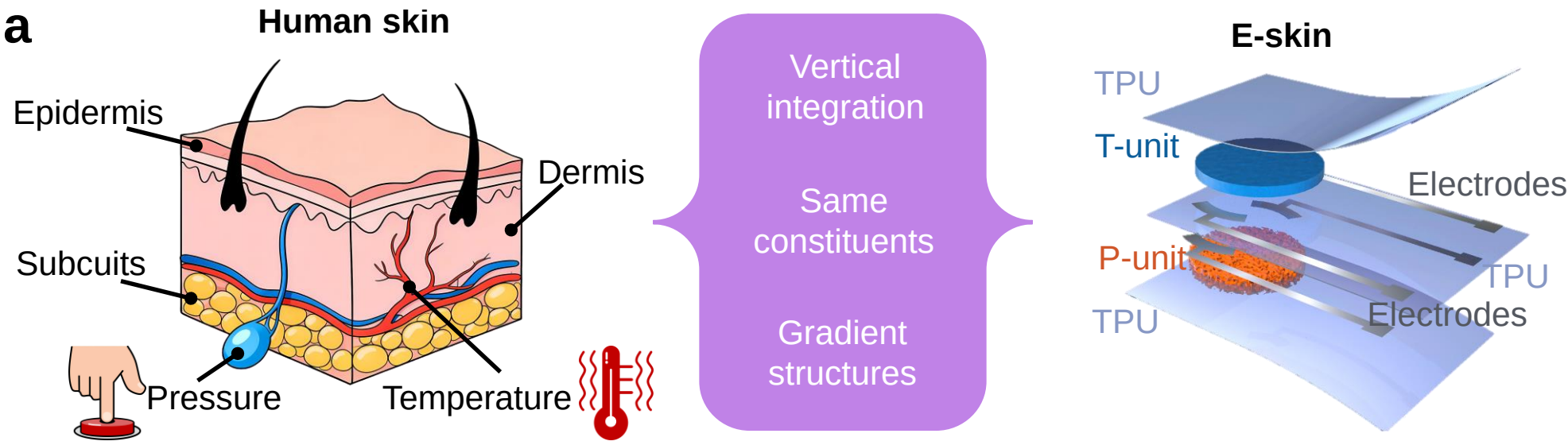
a
Human skin
Epidermis
Dermis
Subcuits
Pressure
Temperature
Vertical integration
Same constituents
Gradient structures
E-skin
TPU
T-unit
Electrodes
P-unit
TPU
TPU
Electrodes

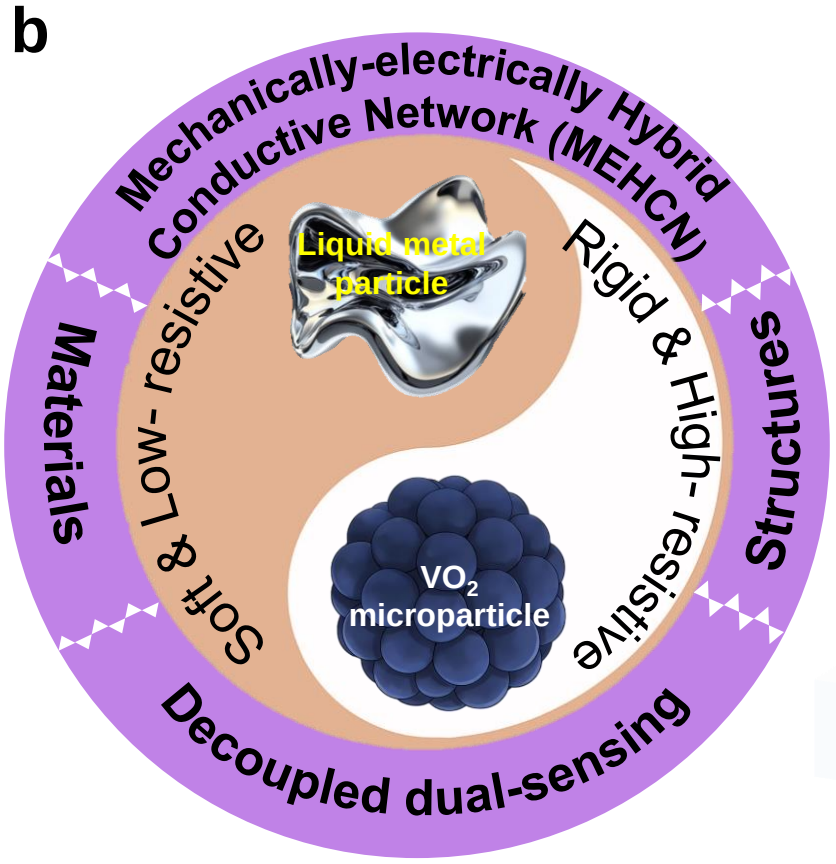
b
Mechanically-electrically Hybrid Conductive Network (MEHCN)
Liquid metal particle
Rigid & High-resistive
Soft & Low- resistive
Materials
Structures
VO2 microparticle
Decoupled dual-sensing

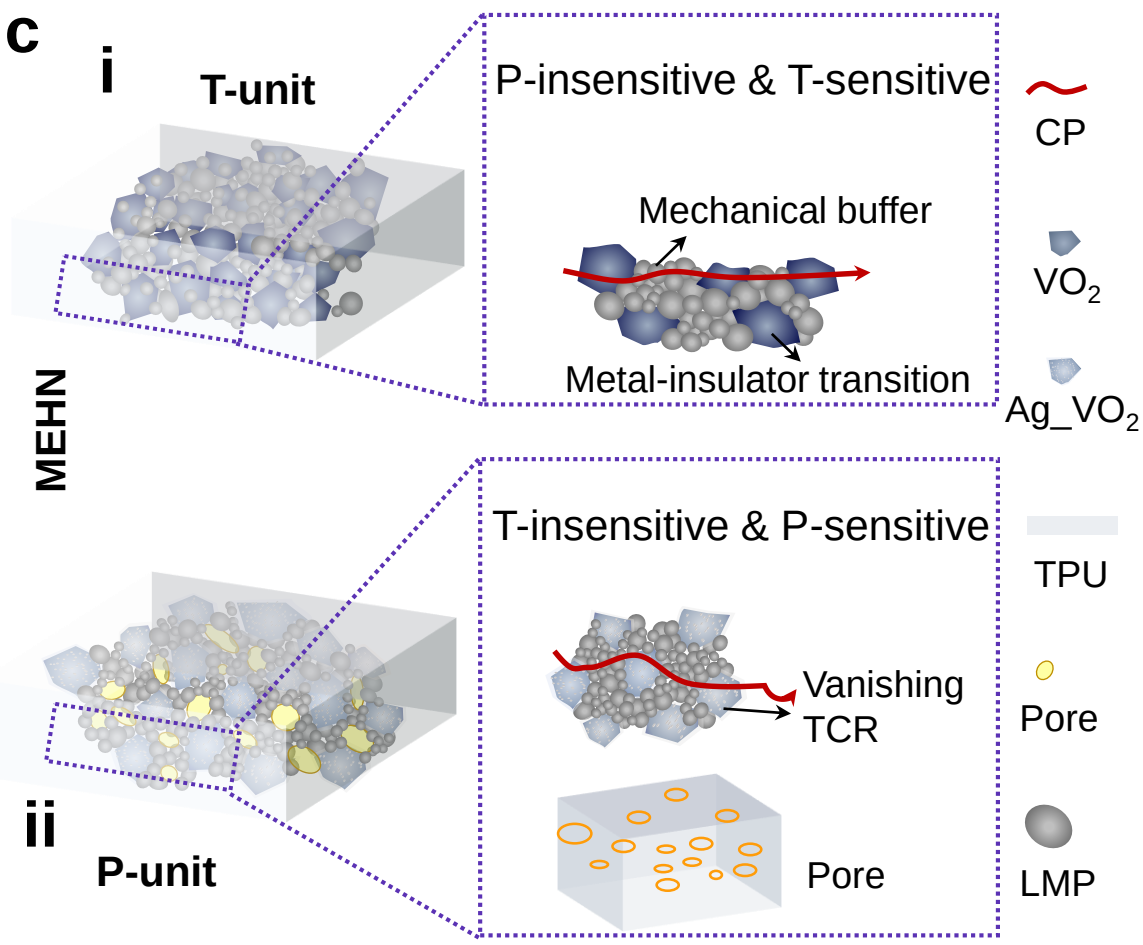
c
i
T-unit
P-insensitive & T-sensitive
Mechanical buffer
Metal-insulator transition
MEHN
T-insensitive & P-sensitive
Vanishing TCR
Pore
ii
P-unit
CP
VO2
Ag_VO2
TPU
Pore
LMP

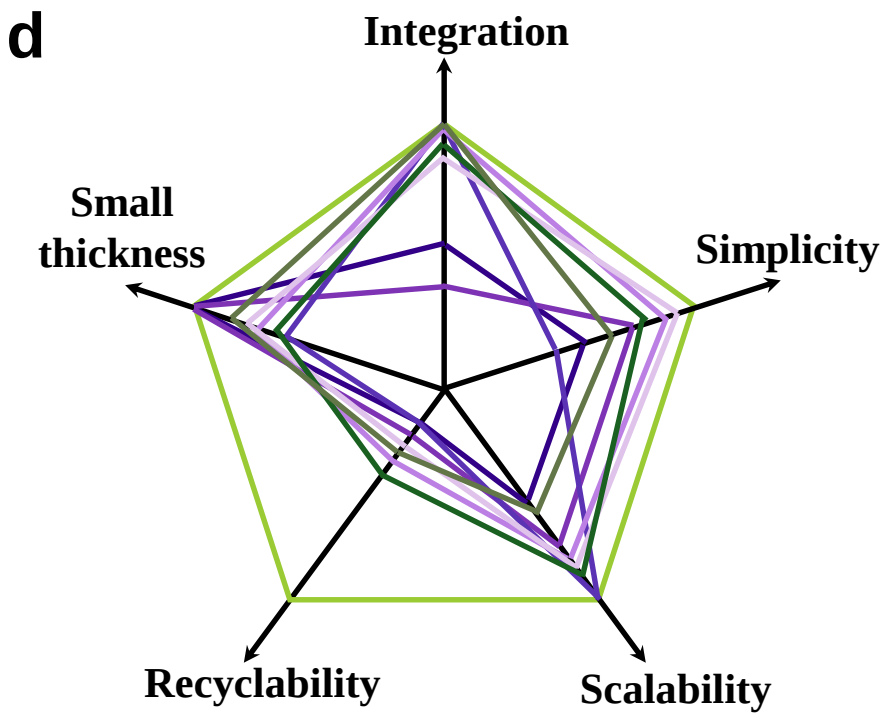
d
Integration
Small thickness
Simplicity
Recyclability
Scalability
10.1126/sciadv.abl8313
10.1021/acsnano.3c04650
10.1002/aisy.202200398
10.1002/advs.202304121
10.1016/j.cej.2023.145475
10.1016/j.snb.2023.135255
10.1002/smll.202307800
This work

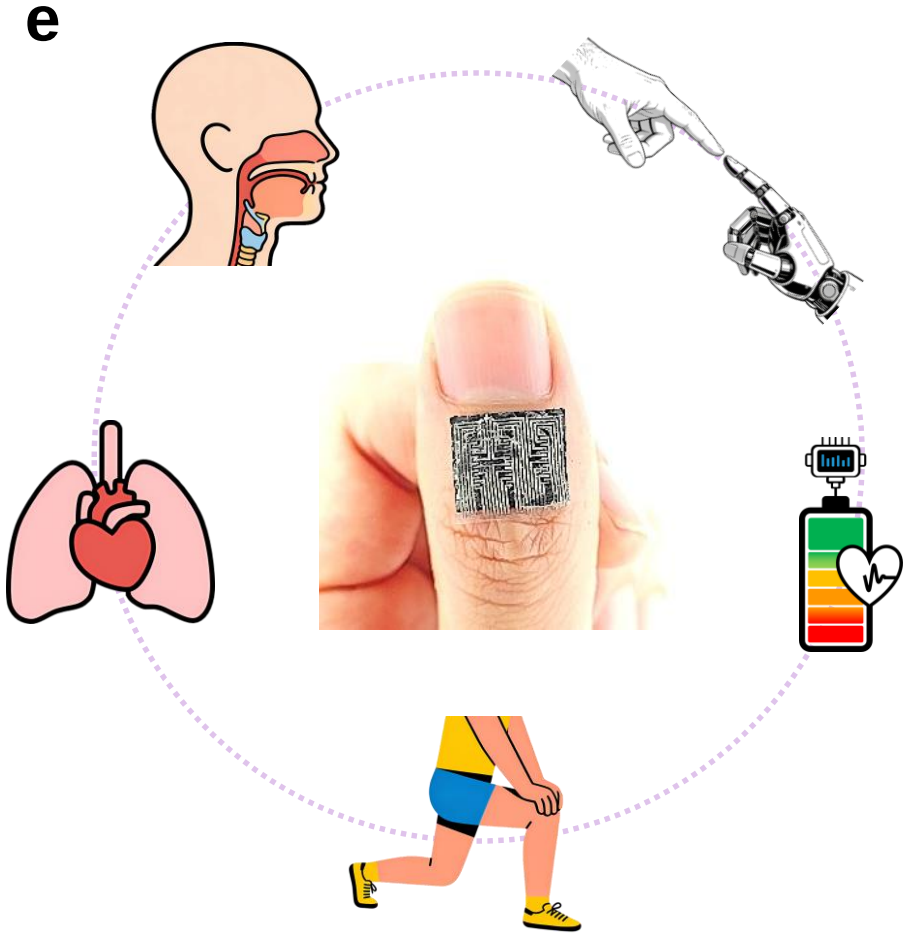
e

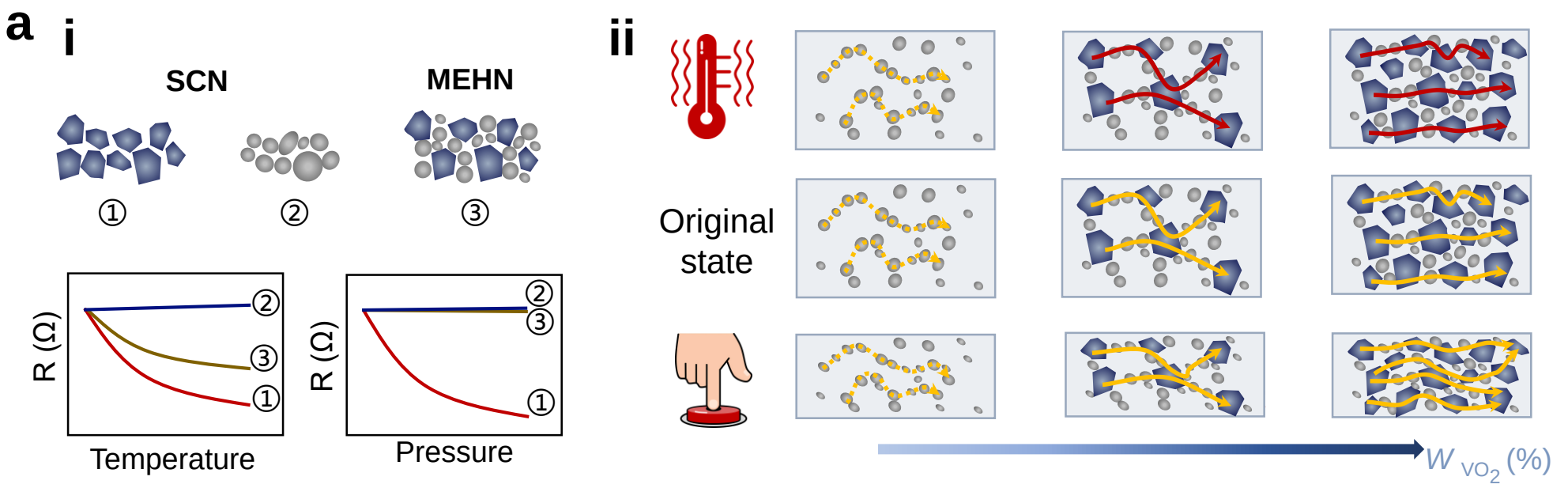
a
i
SCN
MEHN
①
②
③
R (Ω)
Temperature
Pressure
ii
Original state
W_{VO_2} (%)
LMP
VO_2 powder
TPU
High conductive pathways
Low conductive pathways

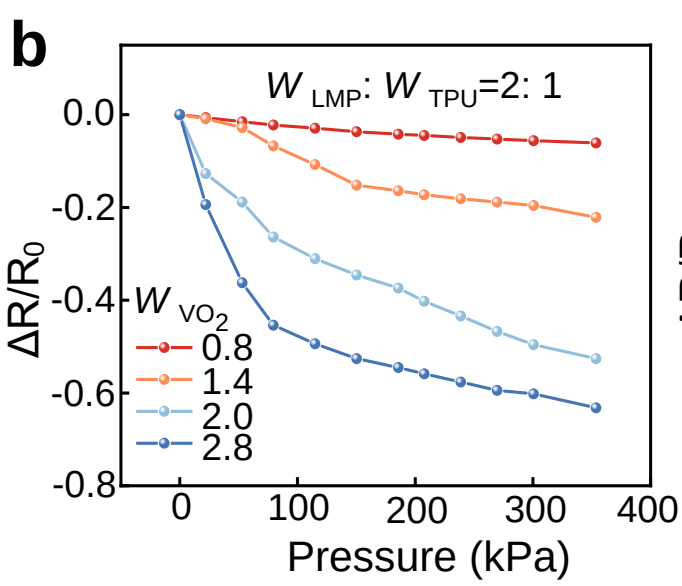
b
W_{LMP}: W_{TPU}=2: 1
W_{VO_2}
0.8
1.4
2.0
2.8
ΔR/R0
Pressure (kPa)

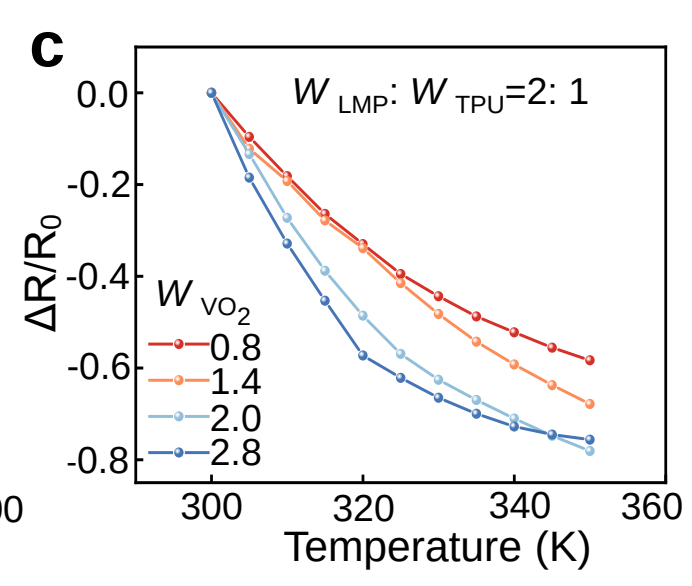
c
W_{LMP}: W_{TPU}=2: 1
W_{VO_2}
0.8
1.4
2.0
2.8
ΔR/R0
Temperature (K)

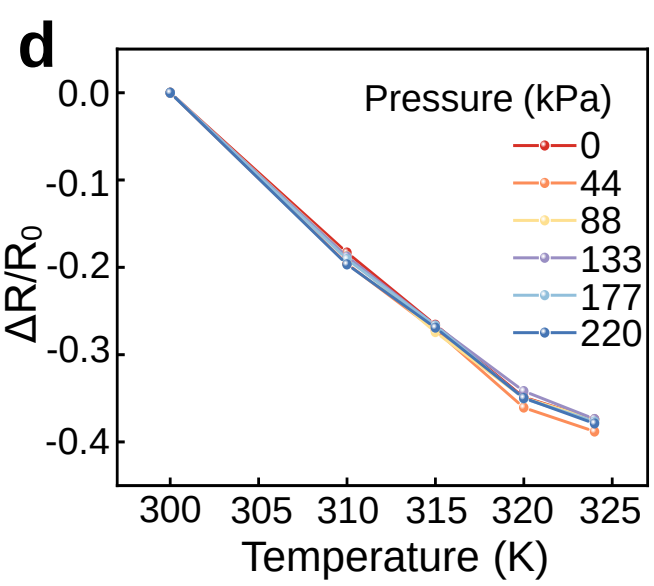
d
Pressure (kPa)
0
44
88
133
177
220
ΔR/R0
Temperature (K)

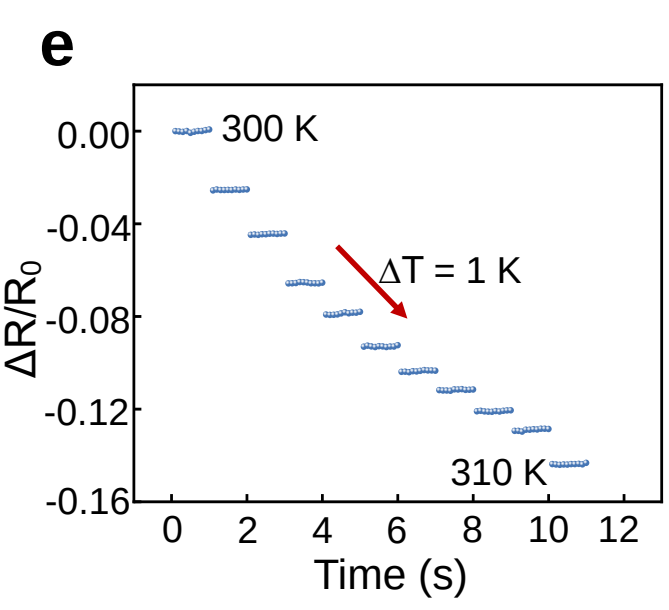
e
300 K
ΔT = 1 K
310 K
ΔR/R0
Time (s)

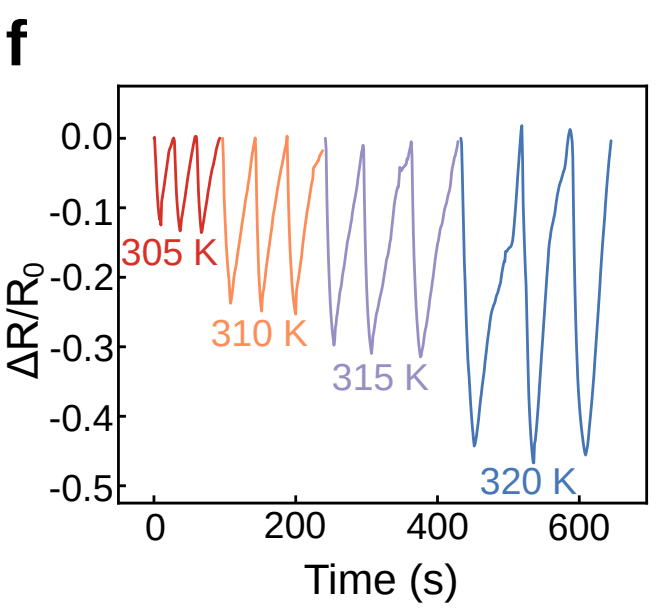
f
305 K
310 K
315 K
320 K
ΔR/R0
Time (s)

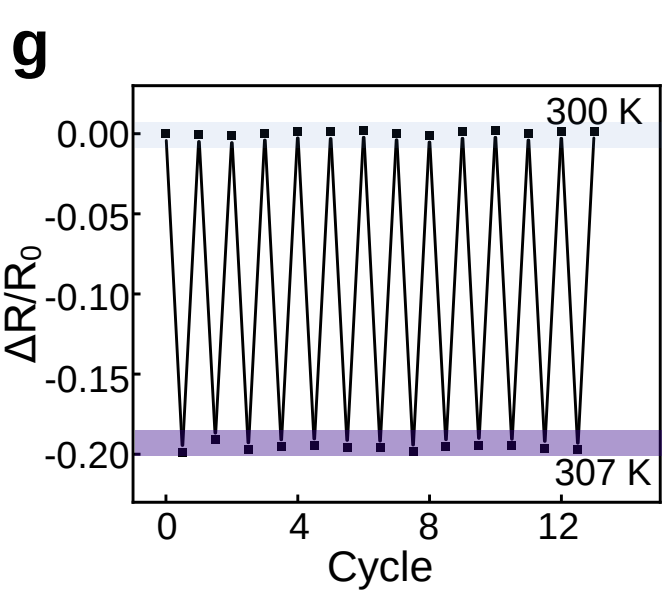
g
300 K
307 K
ΔR/R0
Cycle

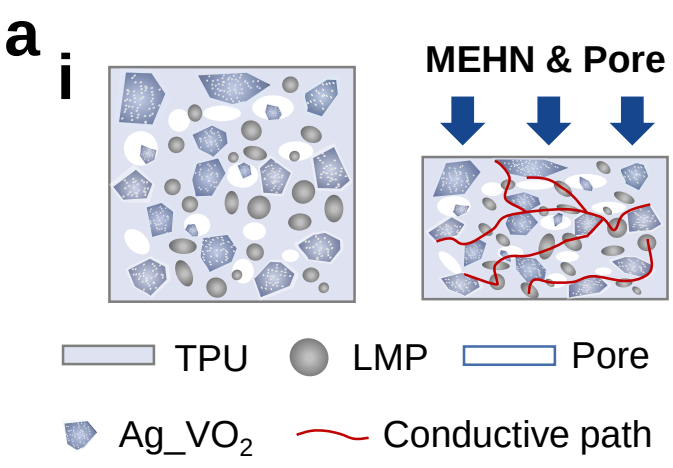
a
i
MEHN & Pore
TPU
LMP
Pore
Ag_VO2
Conductive path

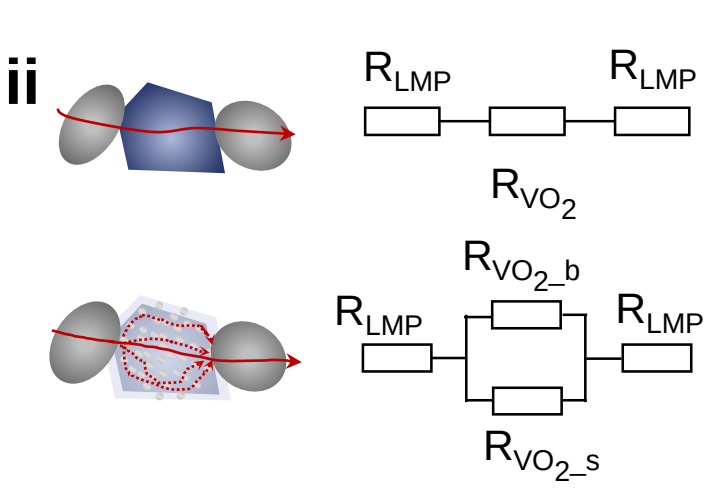
ii
RLMP
RLMP
RVO2
RVO2_b
RLMP
RLMP
RVO2_s

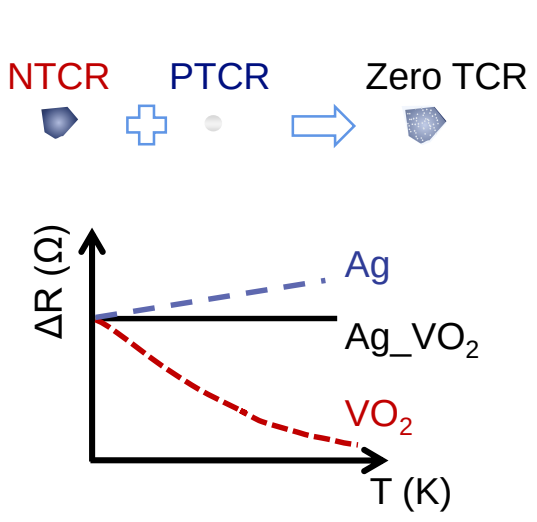
NTCR
PTCR
Zero TCR
ΔR (Ω)
Ag
Ag_VO2
VO2
T (K)

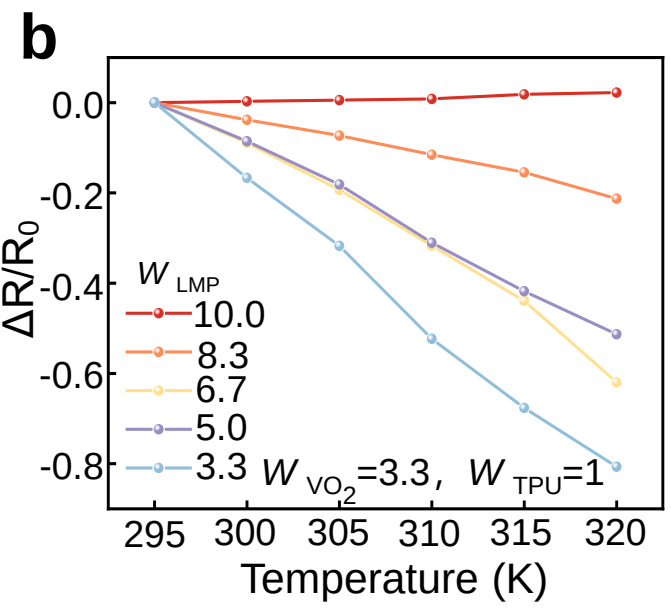
b
ΔR/R0
W LMP
10.0
8.3
6.7
5.0
3.3
W VO2=3.3, W TPU=1
Temperature (K)

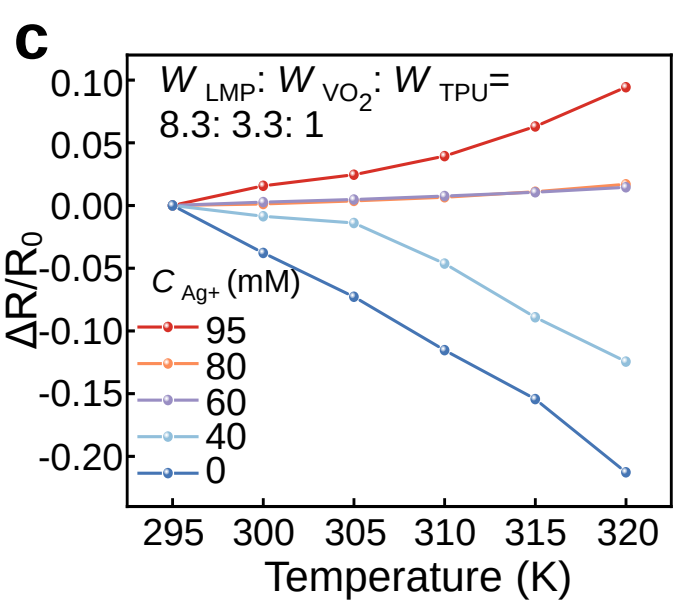
c
W LMP: W VO2: W TPU=
8.3: 3.3: 1
C Ag+ (mM)
95
80
60
40
0
ΔR/R0
Temperature (K)

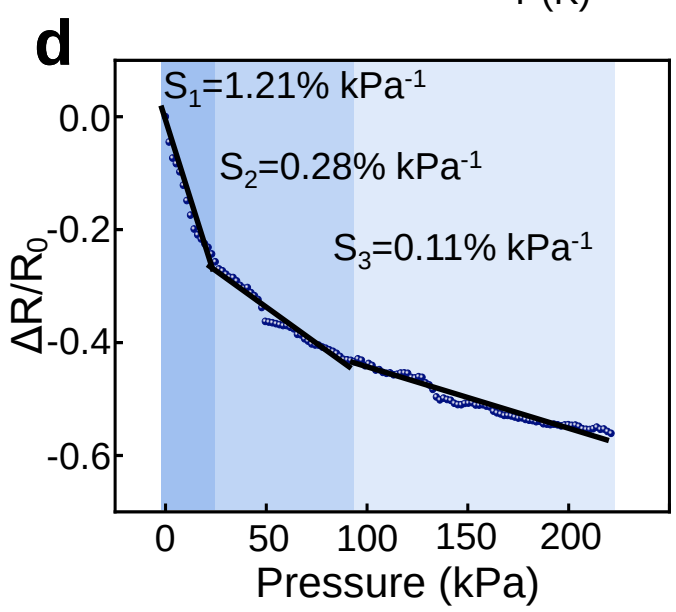
d
S1=1.21% kPa-1
S2=0.28% kPa-1
S3=0.11% kPa-1
ΔR/R0
Pressure (kPa)

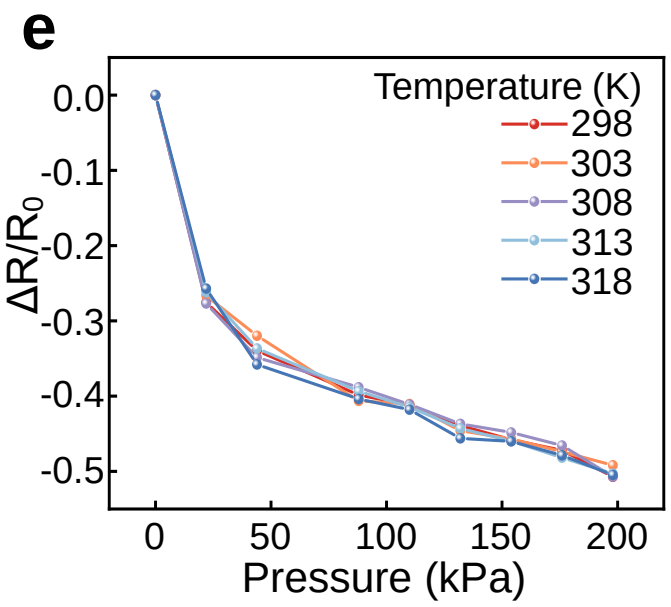
e
Temperature (K)
298
303
308
313
318
ΔR/R0
Pressure (kPa)

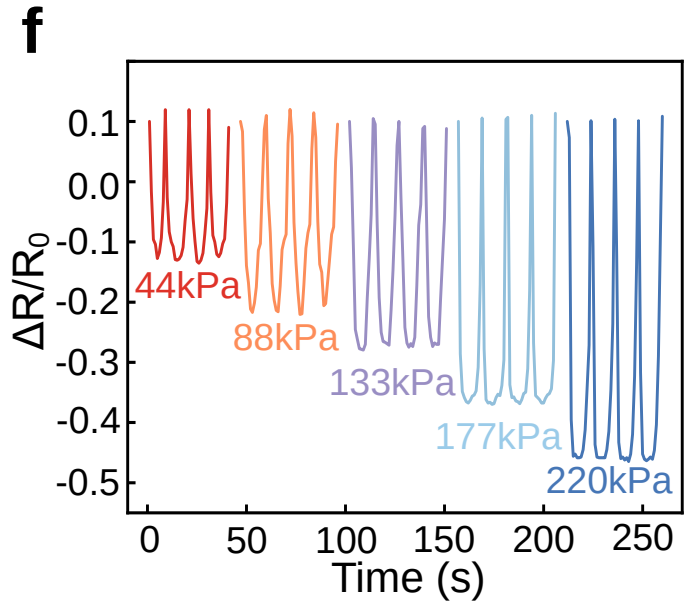
f
44kPa
88kPa
133kPa
177kPa
220kPa
ΔR/R0
Time (s)

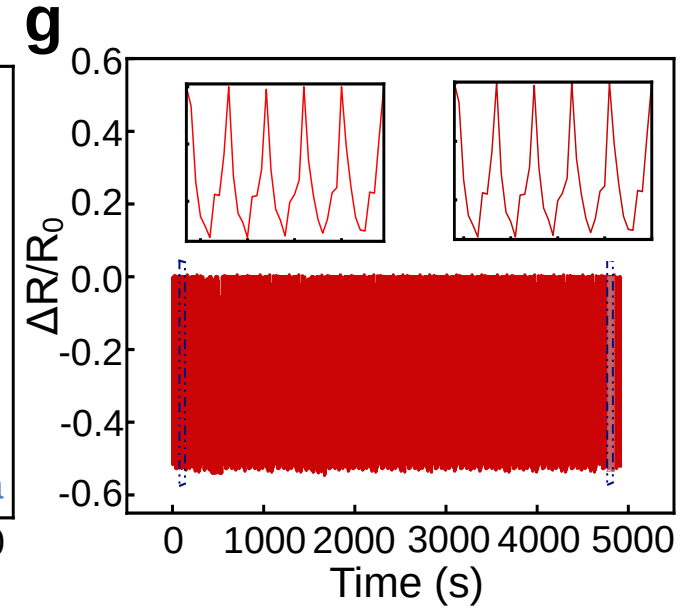
g
ΔR/R0
Time (s)

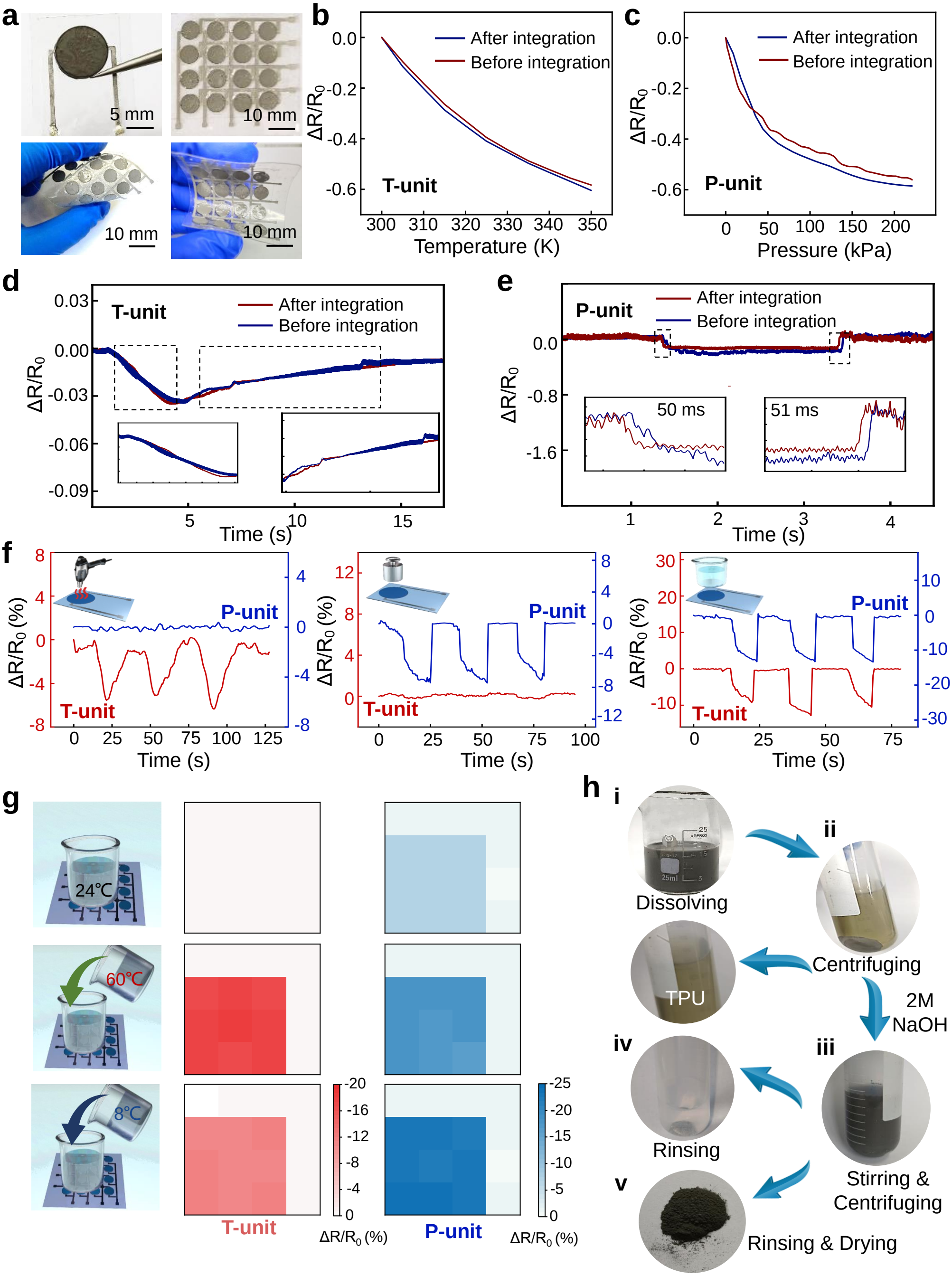
a
5 mm
10 mm
10 mm
10 mm
b
After integration
Before integration
T-unit
ΔR/R0
Temperature (K)
c
After integration
Before integration
P-unit
ΔR/R0
Pressure (kPa)
d
T-unit
After integration
Before integration
ΔR/R0
Time (s)
e
P-unit
After integration
Before integration
50 ms
51 ms
ΔR/R0
Time (s)
f
P-unit
T-unit
ΔR/R0 (%)
Time (s)
g
24°C
60°C
8°C
T-unit
P-unit
ΔR/R0 (%)
h
i
Dissolving
ii
Centrifuging
TPU
2M NaOH
iii
Stirring & Centrifuging
iv
Rinsing
v
Rinsing & Drying

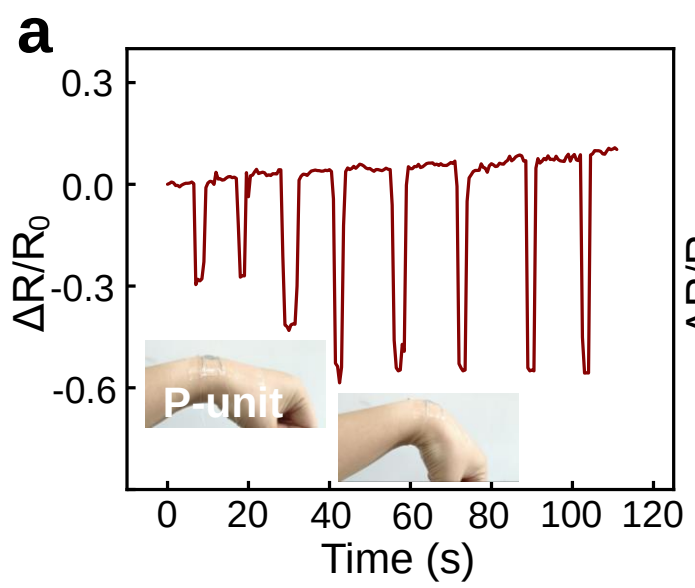
a
ΔR/R0
Time (s)
P-unit

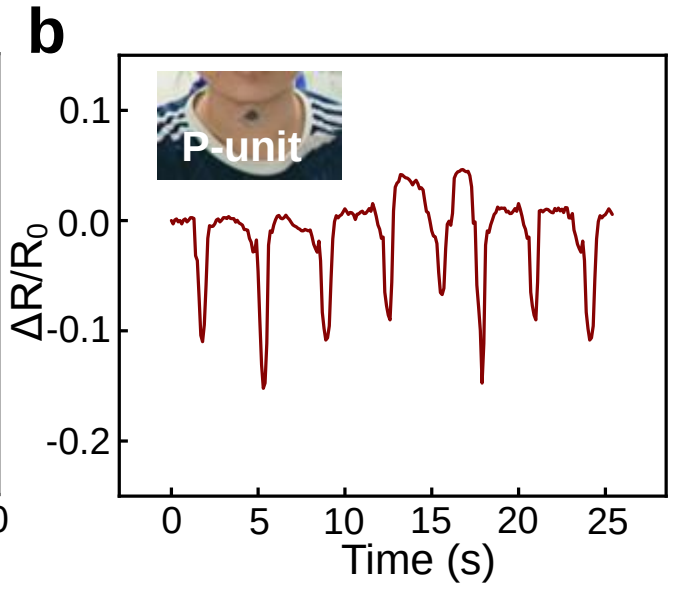
b
ΔR/R0
Time (s)
P-unit

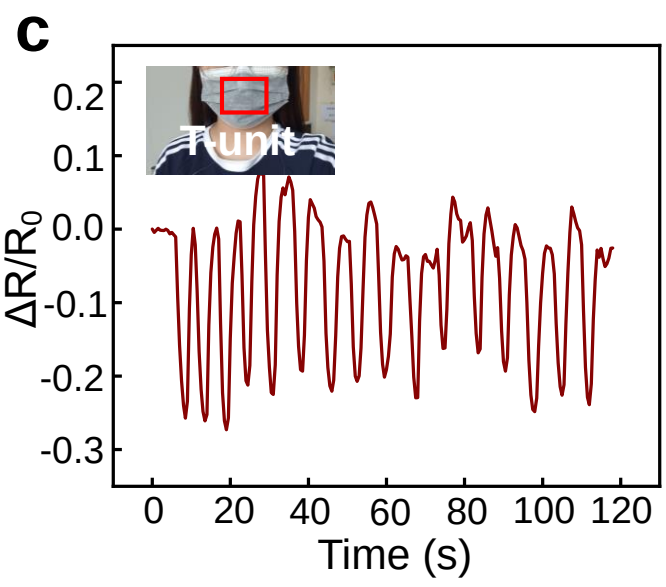
c
ΔR/R0
Time (s)
T-unit

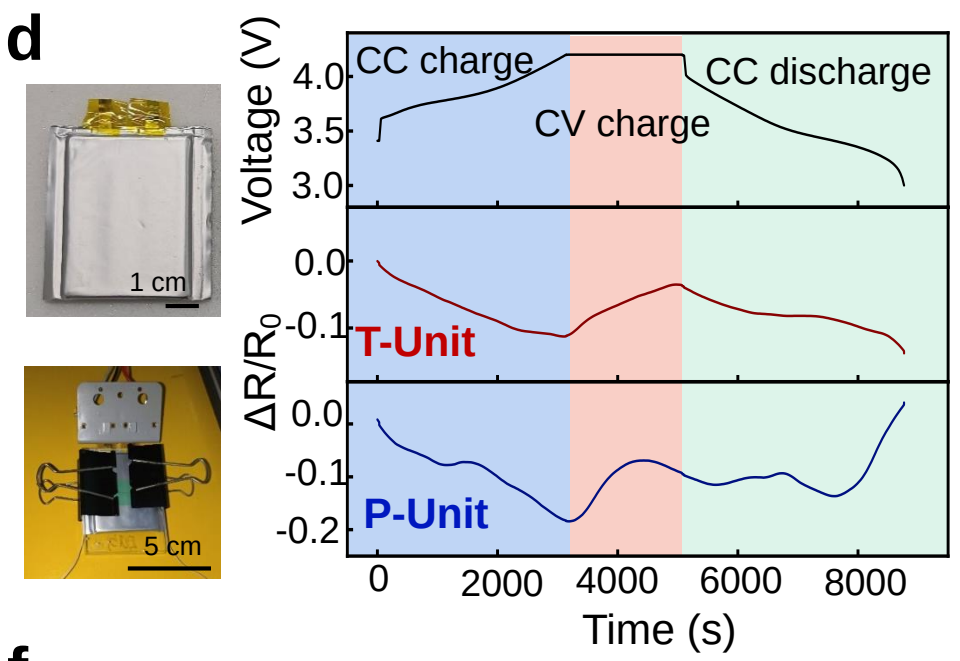
d
1 cm
5 cm
Voltage (V)
CC charge
CV charge
CC discharge
T-Unit
P-Unit
ΔR/R0
Time (s)

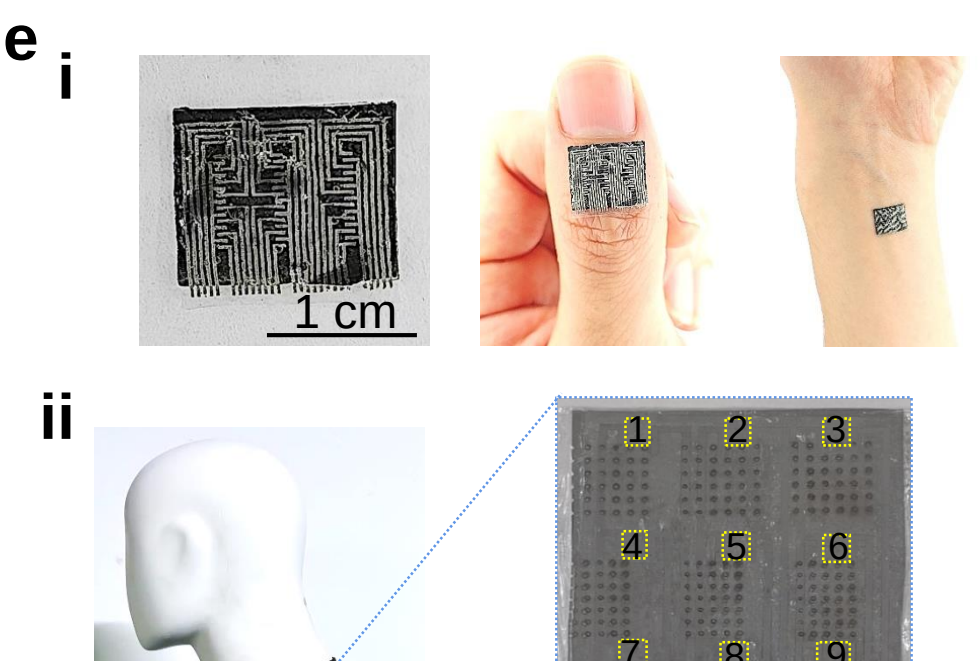
e
i
1 cm
ii
1 2 3
4 5 6
7 8 9
9 mm
1…4 5 6…9 1…456…9
T-unit
P-unit
Flat
Curvy
-0.02
-0.1
ΔR/R0
Time (s)

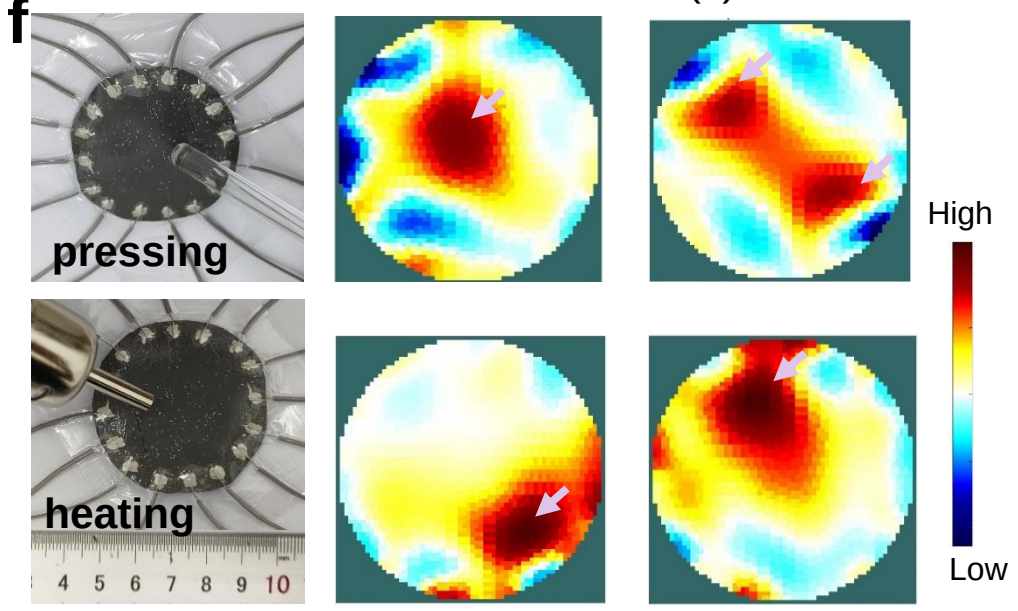
f
pressing
heating
High
Low

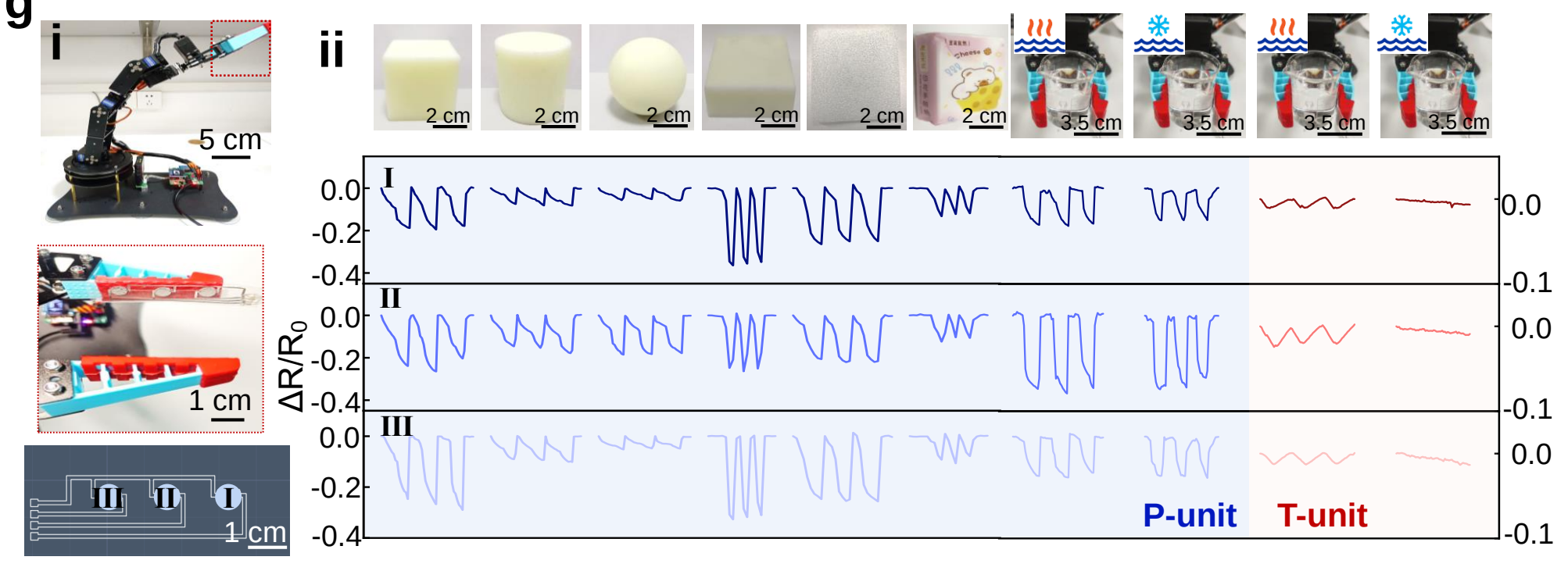
g
i
5 cm
1 cm
1 cm
III II I
ii
2 cm
3.5 cm
I
II
III
ΔR/R0
P-unit
T-unit